Check for updates

Received: 20 March 2025 | Revised: 1 October 2025 | Accepted: 13 November 2025

DOI: 10.1002/qj.70083

Quarterly Journal of the Royal Meteorological Society RMetS

RESEARCH ARTICLE

Characteristics of diabatically influenced cyclones with high wind damage potential in Europe

Svenja Christ[1] | **Julian Quinting**[1,2] | **Joaquim G. Pinto**[1]

[1]Institute of Meteorology and Climate Research Tropospheric Research (IMKTRO), Karlsruhe Institute of Technology (KIT), Karlsruhe, Germany

[2]Institute of Geophysics and Meteorology, University of Cologne, Cologne, Germany

Correspondence
Svenja Christ, Institute of Meteorology and Climate Research Troposphere Research (IMKTRO), Karlsruhe Institute of Technology (KIT), Karlsruhe 76131, Germany.
Email: svenja.christ@kit.edu

Funding information
AXA Research Fund; German Federal Ministry of Research, Technology and Space, Grant/Award Numbers: 01LP1901A, 01LP2322A

ABSTRACT

Extratropical cyclones are the primary driver of midlatitude weather variability, including extreme events with heavy precipitation and severe wind gusts, potentially leading to widespread damage. Both baroclinicity and diabatic heating contribute to cyclone intensification. Examples of severe European winter storms with rapid intensification enhanced through diabatic heating include *Lothar* (1999), *Klaus* (2009), and *Xynthia* (2010). Diabatic heating through cloud condensational processes in extratropical cyclones is associated with the warm conveyor belt (WCB) airstream, among others. Focusing on European winter storms, this study provides a comprehensive assessment of structural differences important for cyclone intensification between cyclones that intensify to a relatively large extent through diabatic processes and cyclones that intensify mostly through baroclinic processes. Considering 247 winter storms affecting western and central Europe from 1979 to 2023, we combine a WCB diagnostic with the pressure tendency equation to quantify the influence of diabatic heating on deepening processes. Our results indicate that diabatic processes have a mean contribution to cyclone intensification of 26.1% (median at 25.3%, 25th and 75th percentiles at 15.2% and 33.4%). Cyclones with a relatively large diabatic influence (> 30.7% diabatic contribution) have similar minimum mean sea-level pressure compared with cyclones with a small diabatic influence (< 20.1% diabatic contribution) but exhibit steeper deepening rates, stronger northward displacement, increased precipitation, stronger wind gusts, and more WCB activity. Moreover, they are characterised by increased moisture and warmer temperatures in the WCB inflow, facilitating stronger deepening rates driven by diabatic heating. Our results suggest that WCB activity is a valuable first indicator of the diabatic contribution to cyclone intensification. These findings may be useful for predicting and estimating the risks associated with winter storms that have a relatively large influence of diabatic processes in numerical weather predictions and climate projections.

KEYWORDS

diabatic heating, European windstorms, extratropical cyclones, high-impact weather, warm conveyor belt

This is an open access article under the terms of the Creative Commons Attribution License, which permits use, distribution and reproduction in any medium, provided the original work is properly cited.
© 2025 The Author(s). *Quarterly Journal of the Royal Meteorological Society* published by John Wiley & Sons Ltd on behalf of Royal Meteorological Society.

1 | INTRODUCTION

Extratropical cyclones are the primary driver of weather variability in the midlatitudes and are often associated with extreme events, including heavy precipitation and severe wind gusts that impact infrastructure, ecosystems, and society (Dowdy & Catto, 2017; Fink *et al.*, 2009; Ulbrich *et al.*, 2009). Given that the impacts can happen simultaneously, these can be seen as compound events. The North Atlantic Ocean basin is a prominent region for the development of extratropical cyclones (Hoskins & Hodges, 2002). Several mechanisms contribute to cyclone intensification: a combination of dynamic and thermodynamic processes driven by baroclinic instability, diabatic heating, upper-level divergence, the jet stream, interactions with potential vorticity (PV) anomalies, and surface heat and moisture fluxes (Schultz *et al.*, 2019; Wernli & Gray, 2024). The strong temperature gradient across the polar-front region, where warm subtropical and cold polar air masses meet, is characterised by strong baroclinicity. In particular, the Gulf Stream region exhibits such an enhanced temperature gradient, creating a zone of high baroclinicity that is essential for cyclogenesis (Gray & Dacre, 2006; Hoskins & Hodges, 2002; Wernli *et al.*, 2002). Baroclinic instability, driven by strong meridional temperature gradients and vertical wind shear, enables the conversion of potential energy to kinetic energy. This conversion and thus cyclogenesis occurs favorably in the equatorward entrance and poleward exit regions of jet streaks that are characterised by upper-tropospheric divergence (Carlson, 1991). During their intensification, some cyclones cross the jet stream from its warm to its cold side and these tend to be the more rapidly deepening cyclones (Baehr *et al.*, 1999).

Diabatic heating from cloud condensation, that is, latent heat release, can be a crucial energy source for storm evolution, increasing the growth rate by reinforcing baroclinic instability (Chang *et al.*, 1982; Danard, 1964; Robertson & Smith, 1983). The vertical distribution of latent heating and the time a storm spends on the equatorward side of the jet stream correlate with its diabatic contribution to deepening (Pirret *et al.*, 2017). Europe is located at the end of the North Atlantic storm track, with a lower cyclone track density than the peak cyclone track density in the central Atlantic (Wernli & Schwierz, 2006; Dacre and Gray, 2009). The rapid development of severe European winter storms, such as *Lothar* (Wernli *et al.*, 2002), *Kyrill* (Fink *et al.*, 2009), and *Xynthia* (Ludwig *et al.*, 2014), has been linked to diabatic heating, indicating a significant contribution of diabatic heating to some extratropical cyclones with severe impact over central Europe.

The airflow through extratropical cyclones can be described in a cyclone-relative framework of airstreams that comprises the warm conveyor belt (WCB), cold conveyor belt, and dry intrusion (Schultz, 2001). The dry intrusion descends behind the cyclone, characterised by cold, dry air forming a comma-shaped cloud-free region (Browning & Roberts, 1994). The cold conveyor belt flows against the cyclone's propagation direction at low levels, with its cyclonic branch often linked to strong winds (Schultz, 2001). The WCB, which is of interest for this study, originates in the lower troposphere in the warm sector of extratropical cyclones and typically ascends poleward ahead of the surface cold front (Wernli, 1997). Due to its large vertical extent, that is, deep ascent, the WCB airstream connects the boundary layer and the upper troposphere in a Lagrangian sense (Wernli, 1997). The WCB is a major driver of cloud formation and precipitation and is thus characterised by substantial latent heat release (Browning, 1990; Madonna *et al.*, 2014). Latent heat release leads to the production of cyclonic PV below the level of maximum heating and a PV reduction above (Madonna *et al.*, 2014; Wernli, 1997). If the PV production occurs close to the cyclone centre, it contributes to cyclone intensification (Binder *et al.*, 2016). In terms of baroclinicity, the latent heat release is associated with a steepening of isentropic surfaces, which leads to locally increased baroclinicity (Joos & Wernli, 2012; Madonna *et al.*, 2014; Wernli, 1997).

Extratropical cyclones can be classified according to different development mechanisms. Cyclone classification includes Type A, driven by frontal wave amplification; Type B, initiated by upper-tropospheric disturbances (Deveson *et al.*, 2002); and Type C, where initial development is dominated by pre-existing upper-level PV anomalies, with mid-tropospheric latent heating sustaining growth (Plant *et al.*, 2003). Primary cyclones generally form along the polar front and are often associated with Type B cyclones (Priestley *et al.*, 2020), while secondary cyclones undergo slightly different mechanisms of cyclogenesis; they can be classified as Type C cyclones (Dacre and Gray 2009; Priestley *et al.*, 2020). While primary cyclones originate from the eastern coast of North America, secondary cyclones typically develop further east of the primary cyclone, over the central and eastern Atlantic, particularly along trailing cold fronts of pre-existing cyclones (Dacre and Gray 2009; Priestley *et al.*, 2020). Such secondary cyclones frequently form during so-called clustered storm periods (Pinto *et al.*, 2014). These cyclones are often associated with pre-existing downstream cyclones, a strong polar jet, and upper-tropospheric cyclonic PV anomalies and lead to extreme events (Stanković *et al.*, 2024). In a warmer climate, the processes involved in cyclone intensification change in different ways that may counteract each other (Catto *et al.*, 2019), but the importance of diabatic processes relevant to cyclone

1477870x, 0, Downloaded from https://rmets.onlinelibrary.wiley.com/doi/10.1002/qj.70083 by Karlsruher Institut Für Technologie, Wiley Online Library on [07/01/2026]. See the Terms and Conditions (https://onlinelibrary.wiley.com/terms-and-conditions) on Wiley Online Library for rules of use; OA articles are governed by the applicable Creative Commons License

intensification is expected to increase. This study aims to quantify the mean contribution of diabatic heating to cyclone intensification in the recent climate, and examines the characteristic structure of cyclones influenced strongly by this process.

The pressure tendency equation (PTE) approach is one way to quantify the diabatic heating contribution to cyclone deepening relative to baroclinic processes (Fink *et al.*, 2012). Diabatic contributions can be substantial in some cases, accounting for up to 60% of deepening and exceeding effects of temperature advection (Pirret *et al.*, 2017). Also, using the PTE approach, Stanković *et al.* (2024) found an increase in the diabatic contribution to cyclone intensification for cyclones associated with extreme wind events over the eastern North Atlantic. However, the relative importance of diabatic and baroclinic processes can vary between storms (Fink *et al.*, 2012; Pirret *et al.*, 2017). As diabatic processes often intensify cyclones (Wernli & Gray, 2024), understanding their relative contribution compared with baroclinic processes systematically is essential for understanding cyclones impacting Europe. Alternative approaches to distinguishing the diabatic and baroclinic contributions to cyclone intensification have been proposed, for example, by Flaounas *et al.* (2021) in the context of Mediterranean cyclones. A key advantage of this method compared with the pressure tendency equation approach is that the diabatic contribution is calculated explicitly rather than as a residual. However, a limitation is that the method requires the implementation of online tracers in the model, making it unsuitable for analyses based on reanalysis data such as the European Centre for Medium-Range Weather Forecasts (ECMWF) Reanalysis Version 5 (ERA5). In addition to diabatic and baroclinic forcing, Flaounas *et al.* (2021) also consider momentum forcing, which can occasionally play a significant role. Also, as WCBs constitute regions of strong latent heat release in extratropical cyclones, studies have emphasised the link between diabatic heating and WCB strength, measured by the number of Lagrangian trajectories that satisfy the criterion of more than 600 hPa ascent within 48 h and cyclone intensification (Binder *et al.*, 2016). Quinting and Grams (2022) have recently developed the machine-learning model (ML-model) EuLerian Identification of ascending AirStreams (ELIAS), which identifies regions of WCB inflow, ascent, and outflow masks on the basis of different atmospheric predictors. The method can be applied to numerical weather prediction and climate model data and offers a computationally efficient alternative to trajectory-based approaches to detect WCBs (Quinting *et al.*, 2022). In this study, we use the PTE approach and combine it with ELIAS to explore the diabatic contribution to cyclone intensification. We investigate systematically the structural differences important for cyclone intensification between cyclones with a relatively large diabatic influence versus a small one. Since cyclones with a relatively large diabatic influence are associated with stronger precipitation, we also consider compound characteristics in terms of wet and windy extremes (Hénin *et al.*, 2021; Pfahl, 2014; Xoplaki *et al.*, 2025; Zscheischler *et al.*, 2020). With a detailed analysis of 247 winter storms impacting central Europe from 1979 to 2023, we address the following research questions.

1. What is the magnitude of the diabatic heating contribution to cyclone intensification in European winter storms?
2. What distinguishes cyclones with a relatively large diabatic influence versus a small one?
3. Do cyclones with a relatively large diabatic influence exhibit stronger WCBs, and can WCB strength indicate the diabatic contribution to cyclone intensification effectively?

The structure of this article is as follows. Data and methods are presented in Section 2. The results are presented in Section 3, followed by a summary and discussion in Section 4.

2 | METHODS

2.1 | Tracking method

To derive cyclone tracks, we apply the algorithm described by Pinto *et al.* (2005) based on Murray and Simmonds (1991) to six-hourly ERA5 reanalysis data from 1979 to 2023 (Hersbach *et al.*, 2020). For the cyclone tracking, we remap from 0.28° to a regular 1° latitude–longitude grid, as the tracking algorithm is optimised for a 1° resolution, and this setup was used in this study. The algorithm is run for the Northern Hemisphere (20°N–90°N) and first identifies the maximum Laplacian of mean sea-level pressure (MSLP), and then finds the MSLP minima closest to it and combines them into a cyclone track. To filter non-synoptic relevant low-pressure centres, a minimum lifetime of 24 h, a minimum intensity (lifetime maximum $\nabla^2 MSLP > 0.6$ hPa · (degree latitude)$^{-2}$), and a minimum deepening rate (maximum $d/dt(\nabla^2 MSLP) \geq 0.3$ hPa · (degree latitude)$^{-2}$ · d^{-1} for a 24-h period) are considered (Pinto *et al.*, 2009). A travel distance of at least 1000 km is required, and cyclones over high orography (1500 m) are discarded. The results of this method compare well with other similar tracking methods (Neu *et al.*, 2013). We further consider only the extended winter season (from September–April), and focus on the 3896 cyclones that reach their peak intensity in the central European region, defined from 42°N–65°N and 10°W–20°E (box in Figure 1). Here, peak intensity is defined as the lowest MSLP during

1477870x, 0, Downloaded from https://rmets.onlinelibrary.wiley.com/doi/10.1002/qj.70083 by Karlsruher Institut Für Technologie, Wiley Online Library on [07/01/2026]. See the Terms and Conditions (https://onlinelibrary.wiley.com/terms-and-conditions) on Wiley Online Library for rules of use; OA articles are governed by the applicable Creative Commons License

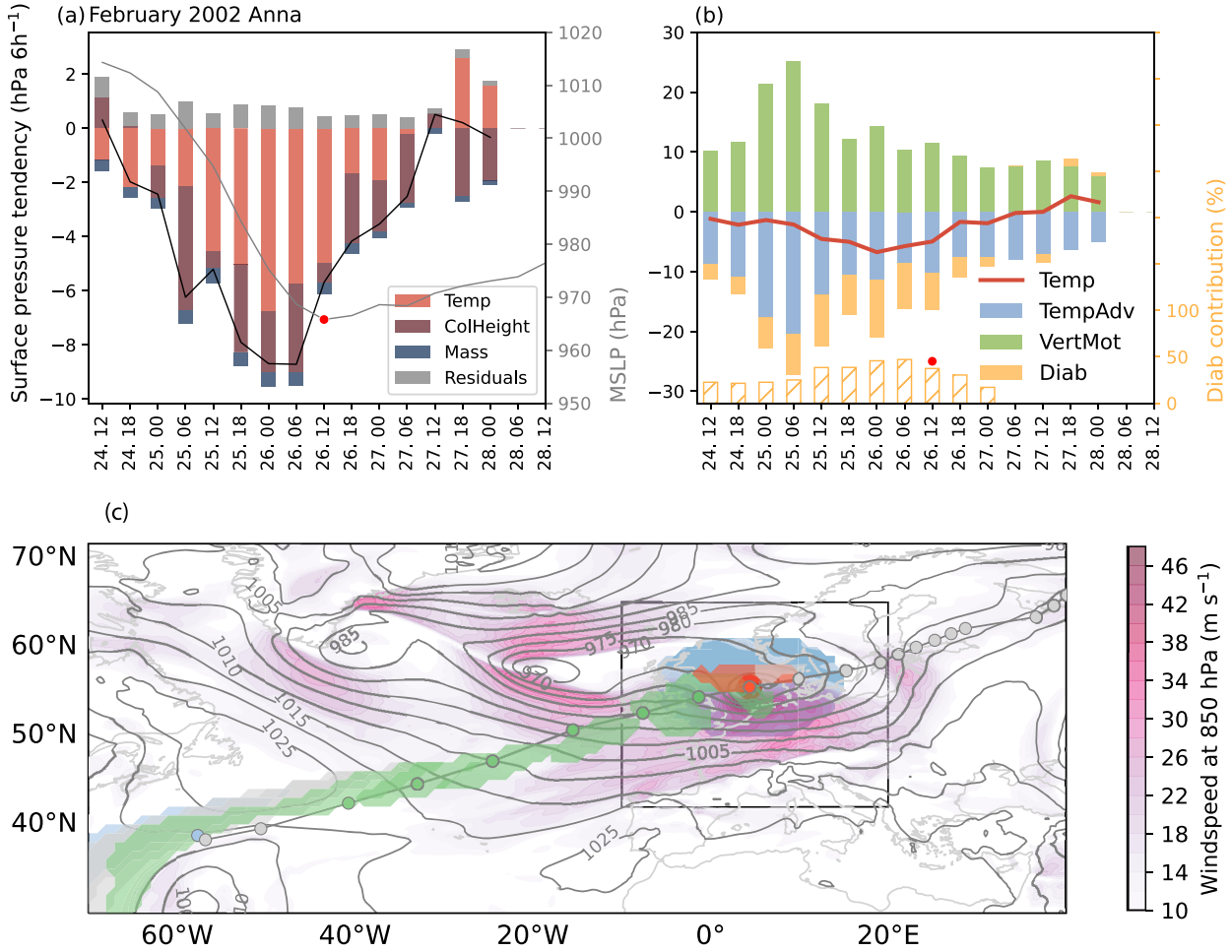

FIGURE 1 Cyclone *Anna* with peak intensity on February 26, 2002. (a) Cyclone track six-hourly and associated WCB ascent masks (from ELIAS) shown from −36 h to 0 h in green, at 0 h in red, and at other times in grey. Wind speed (shading in m · s^{-1} at 850 hPa) and mean sea-level pressure (grey contours, every 5 hPa) at 1200 UTC on February 26, 2002. 700-km radius around the cyclone trackpoint (large blue shading around red cyclone trackpoint) and also the included cyclone track target region (black box, 42°N–65°N and 10°W–20°E). (b) Contributions of temperature tendency (Temp, red bars), geopotential at the upper boundary (ColHeight, dark red bars), mass loss by precipitation (Mass, dark blue bars), and residuals (grey bars) to cyclone deepening (in hPa · (6 h)$^{-1}$, corresponding to Equation 2; see an explanation of the different terms in Section 2.3). Mean sea-level pressure (MSLP) of the cyclone (grey line, in hPa) peak intensity at minimum MSLP (indicated as a red dot). (c) Horizontal temperature advection (TempAdv, blue bars), diabatic heating (Diab, yellow bars), and vertical motion (VertMot, green bars) contributions to cyclone deepening (in hPa · (6 h)$^{-1}$, corresponding to Equation 3). Total temperature tendency (Temp, red line) is the same as Temp from (b). Ratio of diabatic contribution is shown as dashed yellow bars (in %). Peak intensity at minimum MSLP (time marked with red dot). [Colour figure can be viewed at wileyonlinelibrary.com]

the life cycle of the cyclone track. Finally, all cyclone tracks are evaluated relative to the time of their peak intensity, which is defined as 0 h throughout this study. Time steps before peak intensity are indicated as *–xx* h relative to peak intensity.

2.2 | Selection of cyclone tracks impacting Europe

We use the Meteorological Index (MI: Pinto *et al.*, 2012) based on the Klawa and Ulbrich (2003) approach to quantify the severity and thus select the most impactful storms from around 4000 wintertime cyclone tracks with peak intensity over western and central Europe. For the MI, we use a 98th-percentile wind-gust climatology (98thperc) with a threshold for the minimum gust wind speed of 17 m · s^{-1}. This permits the identification of cyclones prone to creating damage:

$$\mathrm{MI} = \left(\frac{\mathrm{wg10m}}{\mathrm{98thperc}}\right)^3, \quad (1)$$

where wg10 is the maximum instantaneous 10-m wind gust in the six-hour time period. The maximum

1477870x, 0, Downloaded from https://rmets.onlinelibrary.wiley.com/doi/10.1002/qj.70083 by Karlsruher Institut Für Technologie, Wiley Online Library on [07/01/2026]. See the Terms and Conditions (https://onlinelibrary.wiley.com/terms-and-conditions) on Wiley Online Library for rules of use; OA articles are governed by the applicable Creative Commons License

instantaneous 10-m wind gusts are taken from the ERA5 within the six-hour time period. The climatology is based on this wind gust information calculated for the extended winter season from 1960 to 2023. For each cyclone track, we identify the time step with the highest MI by aggregating gridpoint-wise MI values over the central European region (42°N–65°N and 10°W–20°E). We rank the cyclone tracks based on these MI values, filter out consecutive daily peaks, and retain only those cyclone tracks where the MI peak occurs within a ±6 h window around the cyclone's peak intensity (per definition also in this region). Finally, we select the 300 highest-ranked cyclone tracks as high-impact cyclones. Because we are interested in physical processes responsible for cyclone intensification, out of the 300 high-impact cyclones, we only consider the cyclone tracks that have an intensification phase of at least −12 h relative to the peak intensity. Therefore, our final sample for a detailed analysis of high-impact cyclones only consists of 247 cyclone tracks. Among the 300 cyclone tracks, 247 extend at least to −12 h relative to the peak intensity, 194 to at least −24 h, and 153 to at least −36 h. One of the reasons for the high proportion of cyclones with a short intensification phase may be the rapid development of cyclones close to Europe (i.e., secondary cyclones: Parker, 1998; Priestley *et al.*, 2020). Moreover, tracking errors may also play a role in some cases. It should be noted that some historical windstorms are missing from our final sample, due to the strict selection criteria and the strong focus on the Central European region (i.e., requiring peak intensity and MI peak within this region). Additionally, some impactful historical cases were excluded because they did not exhibit a −12 h intensification phase. Using the list from Moemken *et al.* (2024) as a reference, some of the storms not included are *Ruzica* (2016), as its peak intensity occurs further west outside our defined region, and cyclone *Zeynep* (2022). However, the results presented in this study show little sensitivity to the selection criteria. We tested different variants of the MI ranking and various time frames for the coincidence of peak intensity and MI peak, and the overall findings remained robust. Additionally, 200 random cyclones were determined from the cyclone tracks. These cyclones are selected randomly from the overall MI ranking. Out of the 200 random cyclones, 165 have an intensification phase of at least −12 h and are taken into account.

2.3 | Diagnosing processes intensifying cyclones: PTE

Cyclone formation is largely influenced by a combination of diabatic processes (radiation and latent heat release) and baroclinic conversion. PTE, as formulated by Knippertz and Fink (2008) and Knippertz *et al.* (2009), can be used to determine the different physical processes that contribute to surface pressure drop (Equation 2). The classical pressure tendency equation is reformulated such that the virtual temperature is the main variable. Following Fink *et al.* (2012), we calculate the PTE terms for each cyclone track, integrate vertically, and average in a 6° × 6° box around the cyclone centre. We apply this approach to a vertical column from the surface to 100 hPa (as in Chen *et al.*, 2024). The ERA5 reanalysis data are available for vertical levels from 50 to 1000 hPa at intervals of 10 hPa. Note that data below the surface are not considered.

$$\underbrace{\frac{\partial p_{\mathrm{sfc}}}{\partial t}}_{\mathrm{Dp}} = \underbrace{\rho_{\mathrm{sfc}} \frac{\partial \phi_{p_2}}{\partial t}}_{\mathrm{ColHeight}} + \underbrace{\rho_{\mathrm{sfc}} R_{\mathrm{d}} \int_{p_{\mathrm{sfc}}}^{p_2} \frac{\partial T_{\mathrm{v}}}{\partial t}\, d\ln p}_{\mathrm{Temp}} + \underbrace{g(E-P)}_{\mathrm{Mass}} + \mathrm{RES}_{\mathrm{PTE}}, \tag{2}$$

$$\mathrm{Temp} = \rho_{\mathrm{sfc}} R_{\mathrm{d}} \left[\underbrace{\int_{p_{\mathrm{sfc}}}^{p_2} -\mathbf{v} \cdot \boldsymbol{\nabla}_p T_{\mathrm{v}}\, d\ln p}_{\mathrm{TempAdv}} + \underbrace{\int_{p_{\mathrm{sfc}}}^{p_2} \left(\frac{R_{\mathrm{d}} T_{\mathrm{v}}}{C_{\mathrm{p}} p} - \frac{\partial T_{\mathrm{v}}}{\partial p} \right) \omega\, d\ln p}_{\mathrm{VertMot}} + \underbrace{\int_{p_{\mathrm{sfc}}}^{p_2} \frac{T_{\mathrm{v}} \dot{Q}}{C_{\mathrm{p}} T}\, d\ln p}_{\mathrm{Diab}} \right] + \mathrm{RES}_{\mathrm{Temp}}, \tag{3}$$

where p_{sfc} is surface pressure, ρ_{sfc} surface air density, ϕ_{p_2} geopotential at p_2 (at 100 hPa), R_{d} the gas constant for dry air, T_{v} the virtual temperature, and g the gravitational acceleration. T is temperature, $\mathbf{v}$ and ω the horizontal and vertical wind components, C_{p} the specific heat capacity at constant pressure, and $\dot{Q}$ the diabatic heating rate.

The surface pressure tendency (Dp, Equation 2) is the sum of (1) the change in the upper boundary geopotential (ColHeight) at 100 hPa, (2) the vertically integrated virtual temperature tendency (Temp), (3) the mass change due to differences of precipitation and evaporation (Mass), and (4) the residuals from errors in data, discretization, and vertical integration. This means that, if the height of an air column remains constant, warming causes the air to expand horizontally, leading to divergence and a reduction in mass within the column, resulting in a drop in surface pressure. Similarly, if only the upper boundary of the column is lowered, the pressure drops, as it must be associated with mass evacuation by divergent winds. The vertically integrated virtual temperature tendency term (Temp from Equation 2) itself is the sum of (1) horizontal temperature advection (TempAdv, that is, baroclinic conversion),

1477870x, 0, Downloaded from https://rmets.onlinelibrary.wiley.com/doi/10.1002/qj.70083 by Karlsruher Institut Für Technologie, Wiley Online Library on [07/01/2026]. See the Terms and Conditions (https://onlinelibrary.wiley.com/terms-and-conditions) on Wiley Online Library for rules of use; OA articles are governed by the applicable Creative Commons License

(2) vertical motion (VertMot, typically associated with rising surface pressure), (3) diabatic heating (Diab), and (4) a residual term. Since ERA5 reanalysis does not provide diabatic heating tendencies explicitly, the Diab term is estimated as the residual by subtracting TempAdv and VertMot from Temp. As a result, the Diab term inevitably includes not only diabatic heating but also residual components arising from the closure of the Temp tendency equation (Equation 3). Although this approach has limitations, tests using explicit heating rates (see auxiliary material in Pohle, 2010; Fink *et al.*, 2012) show that the explicitly calculated Diab term and the Diab term calculated from the residual are usually fairly similar. To quantify the relative contribution of the diabatic heating term to the total virtual temperature pressure tendency (Temp), we calculate the diabatic pressure tendency percentage (Diabptend) following the method of Fink *et al.* (2012), (Equation 4). This approach allows us to quantify the relative contribution of diabatic processes to cyclone intensification compared with TempAdv and VertMot.

$$\text{Diabptend} = \begin{cases} \frac{|\text{Diab}|}{|\text{Temp}|+|\text{VertMot}|+|\text{Diab}|} \times 100, \\ \quad \text{if } \text{sgn}(\text{Diab}) = \text{sgn}(\text{Temp}) = \text{sgn}(\text{VertMot}), \\ \frac{|\text{Diab}|}{|\text{Temp}|+|\text{Diab}|} \times 100, \\ \quad \text{if } \text{sgn}(\text{Diab}) = \text{sgn}(\text{Temp}) \wedge \text{sgn}(\text{Diab}) \\ \qquad \neq \text{sgn}(\text{VertMot}), \\ \frac{|\text{Diab}|}{|\text{VertMot}|+|\text{Diab}|} \times 100, \\ \quad \text{if } \text{sgn}(\text{Diab}) = \text{sgn}(\text{VertMot}) \wedge \text{sgn}(\text{Diab}) \\ \qquad \neq \text{sgn}(\text{Temp}). \end{cases} \tag{4}$$

Finally, we note that the cyclone deepening rate, defined as the change in MSLP along the cyclone track, differs from the quantity Dp, which represents the box-averaged surface pressure change at a fixed location over a six-hour period. As such, a direct equivalence between the two cannot be assumed.

2.4 | WCB identification: ELIAS

To detect WCBs and to evaluate whether cyclones with a relatively large diabatic influence exhibit more pronounced WCB activity, we use the ML-model ELIAS (Quinting & Grams, 2022). The U-Net convolutional neural network predicts conditional probabilities of WCB inflow, ascent, and outflow footprints from instantaneous gridded fields, offering a computationally efficient alternative to trajectory-based approaches (Quinting *et al.*, 2022). In this study, we measure WCB activity in terms of WCB inflow and ascent mask occurrences and size. The WCB inflow is defined as the part of the WCB in the lower troposphere, below 800 hPa, the WCB ascent as the part of the WCB between 800 and 400 hPa, and the WCB outflow the region above 400 hPa. ELIAS is trained for each WCB stage separately and uses a total of five predictors: four are derived from temperature, geopotential height, specific humidity, and the horizontal wind components at 1000, 925, 850, 700, 500, 300, and 200 hPa isobaric surfaces and the fifth is the 30-day running mean trajectory-based climatology of WCB occurrence frequency. ELIAS is verified based on ERA-Interim (Dee *et al.*, 2011) WCB masks retrieved from trajectories that meet the criterion of 600-hPa ascent within 48 h (for more details see Quinting *et al.*, 2022). In this study, the ML-model is applied to ERA5 reanalysis data with a 6 h temporal resolution and remapped from 0.28° to a regular 1° latitude–longitude grid. We repeated some of the analysis with ERA-Interim WCB masks based on trajectories and found the results to be consistent (not shown). To combine the WCB masks with the cyclone tracks, we match the cyclone tracks and WCB masks. We use a radius of 700 km around the cyclone centre to match the WCB mask with the cyclone (average cyclone influence radius: Rudeva & Gulev, 2007, see Figure 1 for an example). Suppose the WCB mask overlaps with at least one grid cell of the radius around the cyclone centre at a given time; this WCB mask is matched to the cyclone trackpoint at that time. The average area of the WCB mask and the averages of different variables in the masks are calculated.

2.5 | Cyclone composites

We use cyclone composites to explore the spatial structures of the cyclones. A radial coordinate system is created for a spherical cap with radii of 9° and 18°. This system is then rotated to align with the cyclone trackpoint at a given time. Following Bengtsson *et al.* (2007) and many others (e.g., Catto *et al.*, 2010; Dacre *et al.*, 2012; Dolores-Tesillos *et al.*, 2022; Priestley & Catto, 2020; Sinclair *et al.*, 2020; Sinclair & Catto, 2023), we interpolate atmospheric variables from the longitude–latitude grid to the radial grid and average over all cyclones in the given cyclone sample group. Cyclones are not rotated in the propagation direction, as we obtained qualitatively similar results when rotating (not shown). In addition, cyclones considered in this study exhibit a similar propagation direction (see Figure 4b).

3 | RESULTS

3.1 | Pressure tendency equation for high-impact cyclones

As a representative case, we investigate the cyclone track of *Anna* from February 2002 with a high MI over central

1477870x, 0, Downloaded from https://rmets.onlinelibrary.wiley.com/doi/10.1002/qj.70083 by Karlsruher Institut Für Technologie, Wiley Online Library on [07/01/2026]. See the Terms and Conditions (https://onlinelibrary.wiley.com/terms-and-conditions) on Wiley Online Library for rules of use; OA articles are governed by the applicable Creative Commons License

Europe, ranking at 70th out of the 300 high-impact cyclone sample. This is indicated by the strong winds (Figure 1a) at 1200 UTC on February 26, 2002, when the cyclone reaches its peak intensity (defined as the lowest MSLP value) of 966 hPa (dot in Figure 1a). The total pressure tendency (Dp in Figure 1b) is highest, with -8.7 hPa $\cdot$ (6 h)$^{-1}$, at -12 h before peak intensity. As shown in Figure 1a, *Anna* is matched (see Section 2.4) with a WCB ascent mask during the entire deepening phase. As described in Section 2.3, the PTE identifies the main processes contributing to cyclone pressure drop. The PTE captures the combined effect of the upper-level lid height changes (ColHeight), mass changes due to precipitation and evaporation (Mass), and vertically integrated changes in virtual temperature (Temp). The amounts of precipitation and evaporation are within a typical range and not unusually small; however, they do not lead to substantial changes in surface pressure. Similar findings regarding these relatively small mass contributions have also been reported by other studies applying the PTE (Fink *et al.*, 2012; Pirret *et al.*, 2017). For this cyclone track, the main contribution to the total pressure change originates from temperature changes (Temp), with values of up to -6.8 hPa $\cdot$ (6 h)$^{-1}$ (Figure 1b). The Temp contribution can be divided further into three components (Figure 1c): temperature advection (TempAdv, baroclinic contribution), diabatic processes (Diab), and vertical motion (VertMot). For this cyclone, the diabatic heating is comparably large, with a maximum contribution of 47% (Figure 1). The WCB ascent masks that can be found continuously during cyclone intensification also reflect the large contribution of diabatic processes, as WCB ascent is associated with diabatic heating in line with Binder *et al.* (2016) and Büeler and Pfahl (2017).

Now we consider all 247 cyclones of our high-impact cyclone sample, where the average pressure tendency, that is, deepening rate (Dp in Figures 2a and 3a) is -7.6 hPa $\cdot$ (6 h)$^{-1}$ at -12 h before the cyclones reach maximum intensity. The average minimum MSLP of all cyclones is 972 hPa (Figures 2a and 3a). Of the three processes contributing to cyclone intensification, the largest average contributor is the change in virtual temperature (Temp). After peak intensity at 0 h, Temp becomes positive, indicating a weakening effect on the cyclones, while the ColHeight and Mass contributions remain negative, continuing to support intensification. Concerning contributions to Temp, the vertical motion term (VertMot) is positive as expected (i.e., weakening the cyclone), while the combined effects of diabatic processes and horizontal temperature advection intensify the cyclone. The median ratio of diabatic heating to the total pressure drop during the intensification phase (from genesis to peak intensity) is 25.3% (Figure 2d), with the 5th and 95th percentiles at 3.4% and 52.6%, respectively. The distribution is skewed towards a lower contribution of diabatic heating, but in some cases exceeds 70%. While horizontal temperature advection is generally the main driver of cyclone intensification, diabatic processes can play a crucial role in certain cases (Figure 2c). The distribution is similar for the random cyclone sample: the median ratio of diabatic heating to the total pressure drop in the intensification phase in the random cyclone sample is 26.1% (Figure 2c), with the 5th and 95th percentiles at 3.3% and 54.4%, respectively. This suggests that the average diabatic contribution of cyclones affecting Europe applies to a wider range of cyclones. In summary, the diabatic contribution to cyclone intensification accounts for approximately one-quarter of the total intensification for a broad range of impactful winter cyclones over central Europe. To explore what distinguishes cyclones with a relatively large diabatic influence from cyclones with a small one, we focus only on the high-impact events.

To examine the differences between more diabatically and more baroclinically driven cyclones, we divide the high-impact cyclone sample into three groups based on the lower and upper terciles of the diabatic contribution ratio distribution during the intensification phase. From now on, we refer to the cyclones with a relatively large contribution of diabatic processes as diabatically driven cyclones and to the cyclones with only a small diabatic influence as baroclinically driven cyclones. The 247 high-impact cyclone tracks are divided into three groups, with 83 cyclones in the lower and upper tercile categories, representing baroclinically driven cyclones in the lower tercile and diabatically driven cyclones in the upper tercile, respectively. The peak intensity, measured as the minimum MSLP, is similar in both groups. Diabatically driven cyclones exhibit a higher deepening rate, with a maximum of -8.6 hPa $\cdot$ (6 h)$^{-1}$, compared with -6.3 hPa $\cdot$ (6 h)$^{-1}$ for baroclinically driven cyclones (Figure 3b). Additionally, the Laplacian of pressure (laplP), which is used to track cyclones, is greater for diabatically driven cyclones than for baroclinically driven ones (Figure 3b). By definition, the diabatic contribution to the intensification of a cyclone is larger in diabatically driven cyclones and the horizontal temperature contribution is smaller (Figure 3c), and vice versa for baroclinically driven cyclones (Figure 3d).

3.2 | Cyclone structures and dynamics

Diabatically driven cyclones develop further south in a warmer and more humid environment along the Gulf Stream front region (Figure 4a). They propagate faster, with an average cyclone propagation speed (-36 h to peak intensity) of 17.1 m $\cdot$ s^{-1} compared with baroclinically

1477870x, 0, Downloaded from https://rmets.onlinelibrary.wiley.com/doi/10.1002/qj.70083 by Karlsruher Institut Für Technologie, Wiley Online Library on [07/01/2026]. See the Terms and Conditions (https://onlinelibrary.wiley.com/terms-and-conditions) on Wiley Online Library for rules of use; OA articles are governed by the applicable Creative Commons License

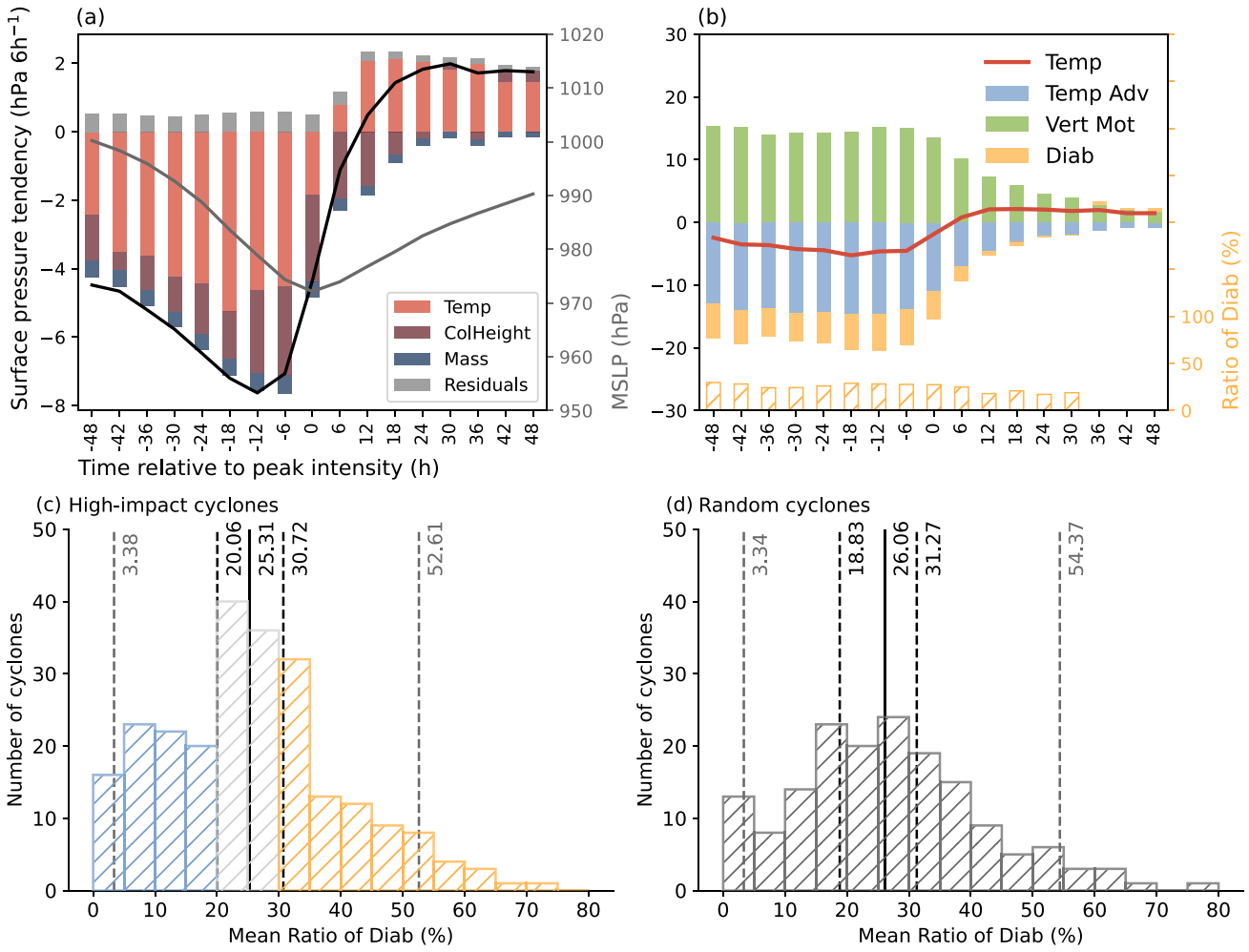

FIGURE 2 (a) Average contributions of temperature tendency (Temp, red bars), geopotential at the upper boundary (ColHeight, dark red bars), mass loss by precipitation (Mass, dark blue bars), and residuals (grey bars) to cyclone deepening (in hPa · (6 h)$^{-1}$), corresponding to Equation 2 (see an explanation of the different terms in Section 2.3) for all 247 high-impact cyclones (Section 2.2). The average mean sea-level pressure (MSLP) of the cyclones (grey line, in hPa) is also shown. (b) Horizontal temperature advection (TempAdv, blue bars), diabatic heating (Diab, yellow bars), and vertical motion (VertMot, green bars) contributions to cyclone deepening (in hPa · (6 h)$^{-1}$) corresponding to Equation 3 for all high-impact cyclones. Total temperature tendency (Temp, red line) same as Temp from (a). Ratio of diabatic contribution shown as dashed yellow bars (in %). (c) Distribution of the average diabatic to total temperature tendency ratio during the cyclone intensification phase of high-impact cyclones. Median (black solid vertical line), terciles (black dashed vertical line), and 5th and 95th percentiles (grey dashed vertical line). Separation into diabatic (orange) and baroclinically driven (blue) cyclones at the lower and upper terciles. (d) Same as (c) but for random cyclones. [Colour figure can be viewed at wileyonlinelibrary.com]

driven cyclones with an average propagation speed of 9.6 m · s^{-}1 (Figure 4b). This holds for each relTime (Figure 4c). Based on this, we can conclude that diabatically driven cyclones are faster and displaced further north. Overall, diabatically and baroclinically driven cyclones differ significantly in location and dynamics. In the cyclone composites (see Section 2.5), a primary cyclone is visible in MSLP contours to the northeast between −36 and −24 h before peak intensity in the diabatically driven cyclone composite (Figure 5b–c), suggesting that the cyclones are secondary cyclones. Diabatically driven cyclones are slightly smaller in size, that is, the region of closed contours is smaller (Figure 5a–d). They experience a more pronounced northward displacement than baroclinically driven cyclones (Figure 4b). Additionally, the composites suggest that they cross the jet stream more often (Figure 5a), whereas baroclinically driven cyclones typically develop and intensify on the polar side (Figure 5e–h). Moreover, diabatically driven cyclones exhibit stronger upper-level divergence (Figure 5b–d) and are characterised by stronger vertical velocities (not shown). All cyclones develop along strong temperature

1477870x, 0, Downloaded from https://rmets.onlinelibrary.wiley.com/doi/10.1002/qj.70083 by Karlsruher Institut Für Technologie, Wiley Online Library on [07/01/2026]. See the Terms and Conditions (https://onlinelibrary.wiley.com/terms-and-conditions) on Wiley Online Library for rules of use; OA articles are governed by the applicable Creative Commons License

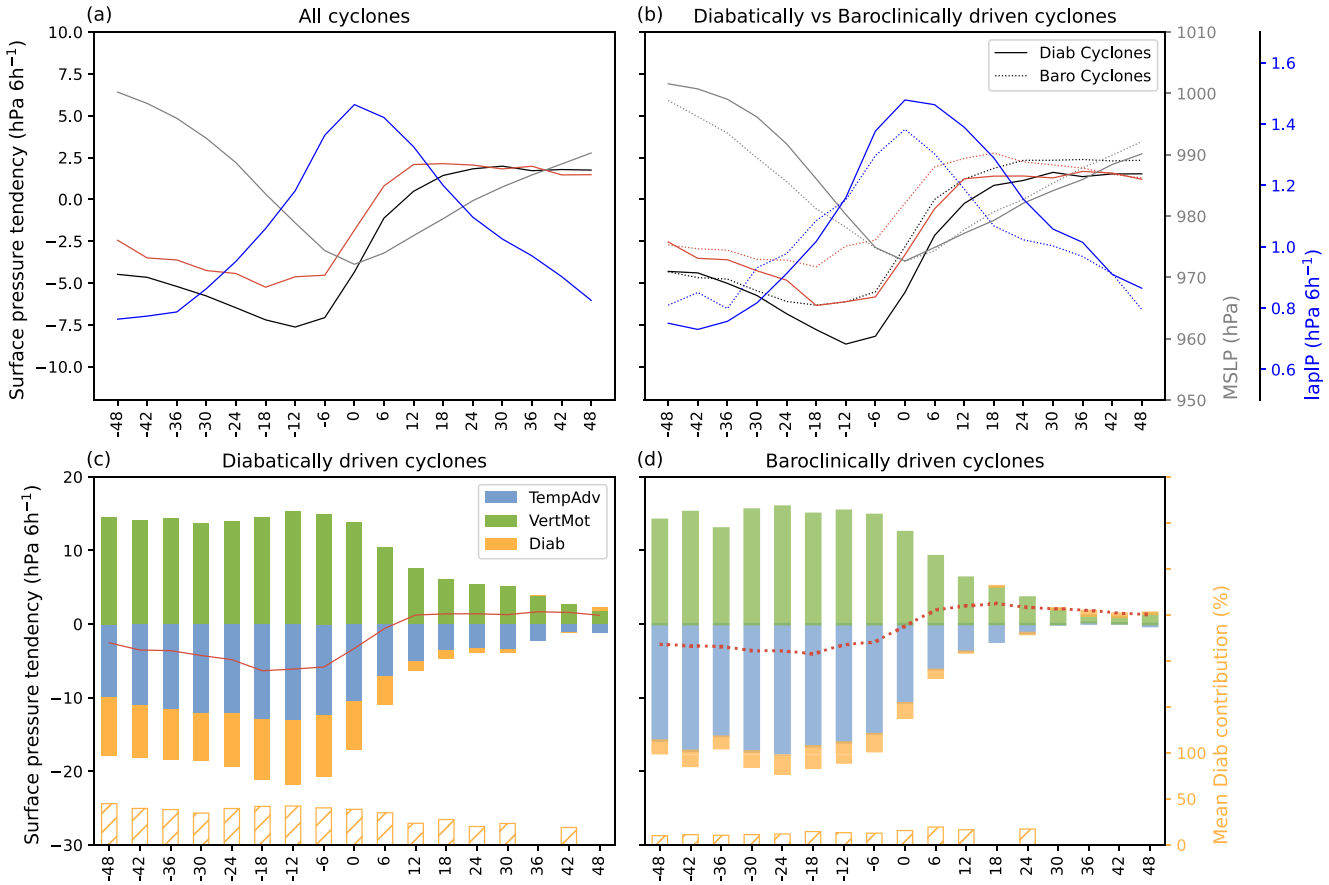

FIGURE 3 (a) Average mean sea-level pressure (MSLP in hPa, grey lines), average pressure tendency (in hPa · (6 h)$^{-1}$, black lines), average Temp term (in hPa · (6 h)$^{-1}$, red lines), and average Laplacian of MSLP (laplP, in hPa · (6 h)$^{-1}$, blue lines) for all 247 high-impact cyclones. (b) same as (a) but for diabatically driven tercile (solid lines) and baroclinically driven tercile (dashed lines) cyclones. (c,d) Same as Figure 2b, but for diabatically driven and baroclinically driven cyclones, respectively. [Colour figure can be viewed at wileyonlinelibrary.com]

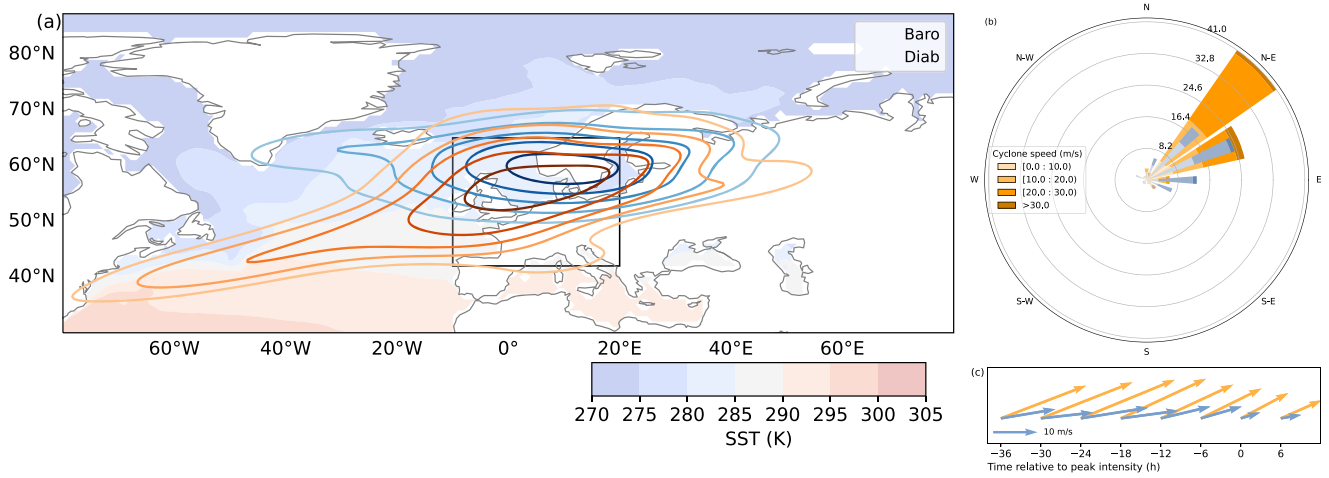

FIGURE 4 (a) Cyclone track density (contours at 30, 45, 60, 75, 90%), for diabatically driven (Diab, orange contours) and baroclinically driven (Baro, blue contours) cyclones. Sea-surface temperature extended wintertime climatology from 1979 to 2023 (shading, in K). Cyclone track target region (black box, 42 to 65°N and 10°W to 20°E). (b) Cyclone propagation speed and direction (absolute speed in m · s^{-1} and direction from −36 h to peak intensity) for diabatically driven (orange) and baroclinically driven (blue) cyclones. (c) Cyclone propagation speed and direction (speed in m · s^{-1} and direction) for diabatically driven (orange) and baroclinically driven (blue) cyclones. [Colour figure can be viewed at wileyonlinelibrary.com]

1477870x, 0, Downloaded from https://rmets.onlinelibrary.wiley.com/doi/10.1002/qj.70083 by Karlsruher Institut Für Technologie, Wiley Online Library on [07/01/2026]. See the Terms and Conditions (https://onlinelibrary.wiley.com/terms-and-conditions) on Wiley Online Library for rules of use; OA articles are governed by the applicable Creative Commons License

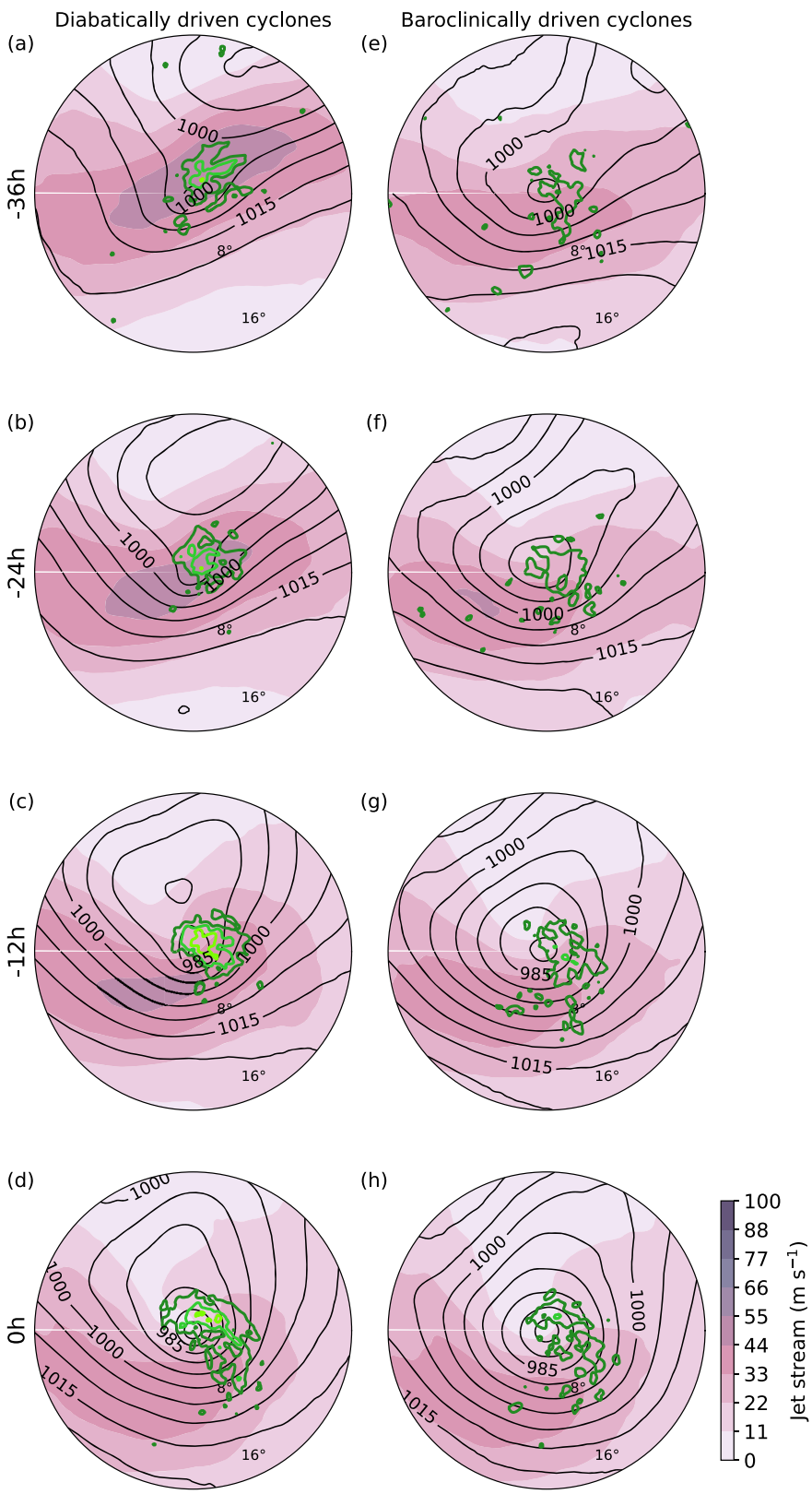

FIGURE 5 Cyclone composites of jet stream (shading in $m \cdot s^{-1}$ at 300 hPa), mean sea-level pressure (black contours, every 5 hPa), and divergence at 300 hPa (green contours at 1, 2, 3×10^5 s^{-1}) for diabatically driven (left column) and baroclinically driven (right column) cyclones at −36, −24, −12, and 0 h relative to peak intensity with a 18° radius around the cyclone centre. [Colour figure can be viewed at wileyonlinelibrary.com]

gradients. During the deepening phase, the equivalent potential temperature contours are closer to each other in the diabatically driven cyclone composites compared with the baroclinically driven cyclone composites (Figure 6a–c). Baroclinically driven cyclones develop in regions with a lower temperature gradient; despite our expectation that they would form in areas with strong horizontal temperature gradients, their development in areas with

1477870x, 0, Downloaded from https://rmets.onlinelibrary.wiley.com/doi/10.1002/qj.70083 by Karlsruher Institut Für Technologie, Wiley Online Library on [07/01/2026]. See the Terms and Conditions (https://onlinelibrary.wiley.com/terms-and-conditions) on Wiley Online Library for rules of use; OA articles are governed by the applicable Creative Commons License

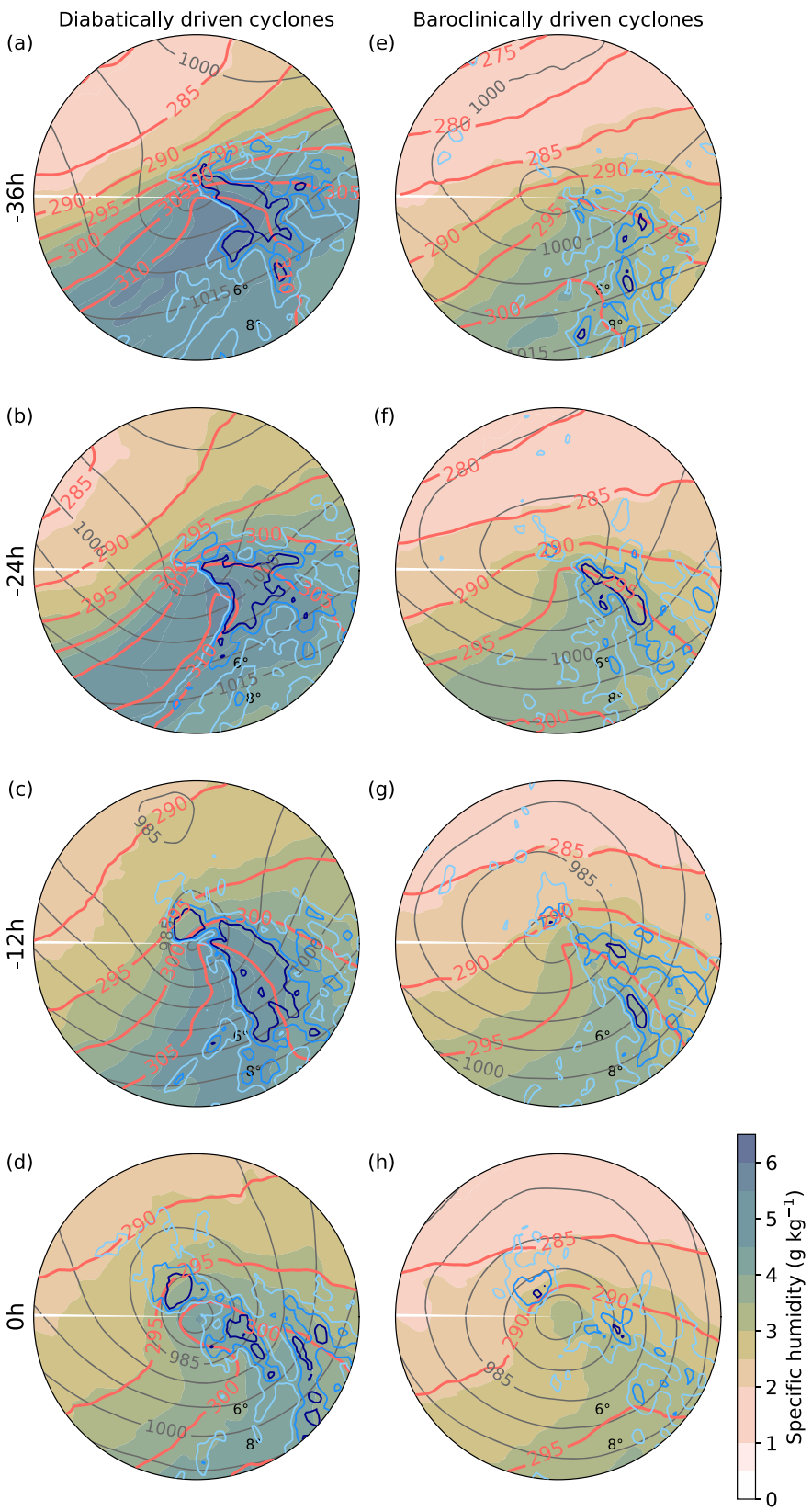

FIGURE 6 Cyclone composites for specific humidity at 850 hPa (shading, in $g \cdot kg^{-1}$), equivalent potential temperature at 850 hPa (red contours, every 5 K), moisture flux convergence at 850 hPa (blue contours at −1.5, −1, -0.5×10^{-4} $g \cdot kg^{-1}$ s^{-1}), and mean sea-level pressure (black contours, every 5 hPa) for diabatically driven (left column) and baroclinically driven (right column) cyclones at −36, −24, −12, and 0 h relative to peak intensity with a 9° radius around the cyclone centre. [Colour figure can be viewed at wileyonlinelibrary.com]

lower temperature gradients may explain their lower deepening rates. Higher potential temperature gradients would be expected for baroclinically driven cyclones with similar deepening rates. Also, a larger proportion of diabatically driven cyclones develop in the Gulf Stream region, characterised climatologically by a higher potential temperature gradient. Additionally, enhanced diabatically induced heating in the diabatically driven cyclones

1477870x, 0, Downloaded from https://rmets.onlinelibrary.wiley.com/doi/10.1002/qj.70083 by Karlsruher Institut Für Technologie, Wiley Online Library on [07/01/2026]. See the Terms and Conditions (https://onlinelibrary.wiley.com/terms-and-conditions) on Wiley Online Library for rules of use; OA articles are governed by the applicable Creative Commons License

may have steepened the isentropic surfaces and enhanced baroclinicity. Furthermore, the warm core at peak intensity time in Figure 6 suggests that diabatically driven cyclones are primarily Shapiro–Keyser cyclones, in contrast to baroclinically driven cyclones, which appear to be closer to the Norwegian cyclone structure. These differences emphasise the contrasting dynamics driving the evolution of diabatically and baroclinically driven cyclones.

3.2.1 | Moisture availability

Moisture availability is an important precondition for latent heat release and cyclone intensification (Chen *et al.*, 2024; Demirdjian *et al.*, 2023). In our study, diabatically driven cyclones evolve in a significantly more humid environment (Figure 6a–c). This is particularly evident during the deepening phase at −36 and −12 h, when diabatically driven cyclones exhibit higher specific humidity compared with baroclinically driven cyclones. In the warm sector of diabatically driven cyclones, the average specific humidity exceeds 5 $g \cdot kg^{-1}$. The differences in specific humidity (not shown) between diabatically driven and baroclinically driven cyclones are statistically significant at all time steps tested with bootstrapping. This enhanced humidity is likely due to their development further south, often over warmer sea-surface temperatures in the Gulf Stream region. Additionally, diabatically driven cyclones show stronger moisture flux convergence, especially in the early stages of intensification, compared with baroclinically driven cyclones (Figure 6a–c). In summary,

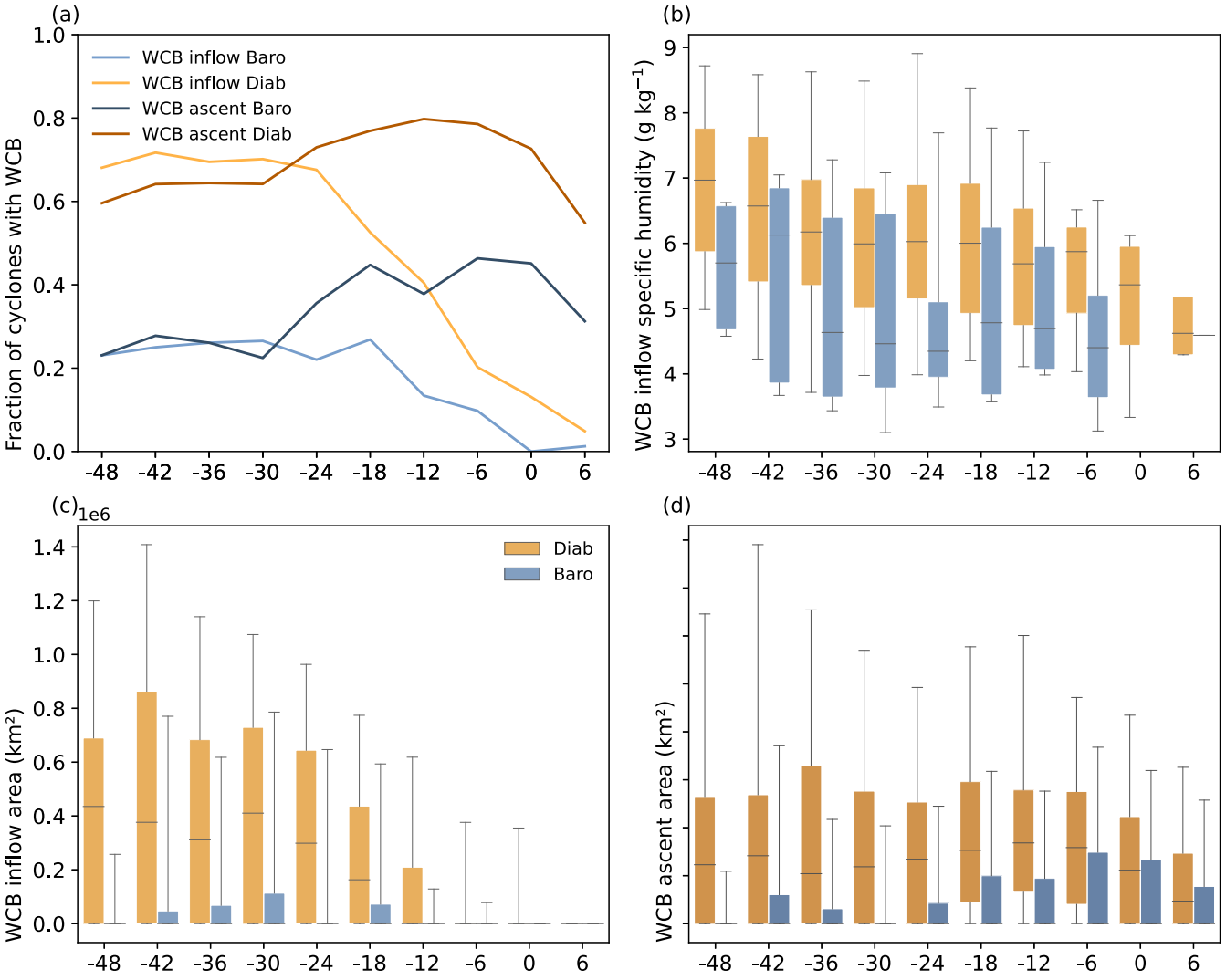

FIGURE 7 (a) Fraction of cyclones that have WCB inflow and ascent regions associated with cyclone tracks for diabatically driven (orange) and baroclinically driven (blue) cyclones. (b) Average specific humidity (in $g \cdot kg^{-1}$) in WCB inflow associated with diabatically driven (Diab, orange) and baroclinically driven (Baro, blue) cyclone tracks. (c) Average WCB inflow area (in km^2) associated with diabatically driven (orange) and baroclinically driven (blue) cyclone tracks. (d) Same as (c) but for WCB ascent area. [Colour figure can be viewed at wileyonlinelibrary.com]

1477870x, 0, Downloaded from https://rmets.onlinelibrary.wiley.com/doi/10.1002/qj.70083 by Karlsruher Institut Für Technologie, Wiley Online Library on [07/01/2026]. See the Terms and Conditions (https://onlinelibrary.wiley.com/terms-and-conditions) on Wiley Online Library for rules of use; OA articles are governed by the applicable Creative Commons License

diabatically driven cyclones develop in a more humid environment, which likely promotes stronger diabatic heating and cyclone intensification.

3.3 | Warm conveyor belts

Next, we analyse the area of WCB masks and the physical conditions in the WCB inflow region. We argue that the area of the WCB masks can be used as a first proxy for WCB strength, as the area indirectly represents the volume of ascending air, that is, the larger the WCB mask, the more widespread the ascent. The ML-model ELIAS detects WCBs more frequently for diabatically driven cyclones than for baroclinically driven cyclones (Figure 7a). The ratio of diabatically driven cyclones associated with a WCB inflow mask reaches up to 0.71 and that for WCB ascent up to 0.80, while baroclinically driven cyclones show lower ratios of 0.27 and 0.46, respectively (Figure 7a). This does not imply that there are no WCBs; rather, it suggests that the WCB is too weak to meet the criterion for WCB detection. As expected, the WCB inflow area peaks earlier (−36 to −18 h) compared with the WCB ascent area, which peaks between −12 and −6 h. Moreover, diabatically driven cyclones are associated with larger WCB inflow and ascent areas compared with baroclinically driven cyclones, particularly during the earlier stages of intensification (Figure 7c–d). This indicates stronger vertical upward mass flux for diabatically than for baroclinically driven cyclones. The larger WCB inflow areas in diabatically driven cyclones are accompanied by higher average specific humidity (Figure 7b) and equivalent potential temperature (not shown) within the WCB inflow mask. The median values range from 4.75–7 $g \cdot kg^{-1}$ for specific humidity and 300–317 K for equivalent potential temperature, both of which are higher in diabatically driven cyclones compared with baroclinically driven ones. These differences are most pronounced during the early development phase, when WCB inflow occurrence is more frequent. Notably, these results include only cyclones with an associated WCB mask (see Section 2.4). These findings align with the more moist environments in which diabatically driven cyclones are found to develop (Section 3.2.1) and enhanced moisture availability might be a reason for more pronounced WCB activity. Higher WCB inflow frequencies are highlighted further in Figure 8, where WCB inflow frequencies are more pronounced at −36 and −24 h (Figure 8a–b), WCB ascent from −24 to −12 h (Figure 8b–c), and the WCB outflow peak at −12 and 0 h (Figure 8c–d). Additionally, the location of the WCB inflow downstream of the cyclone centre in Figure 8a,b indicates that the inflow originates from the environment into which the cyclone is propagating. This is consistent with the feeder airstream concept, in which air ahead of the cyclone flows into the ascending WCB (Dacre *et al.*, 2019). In summary, diabatically driven cyclones are more frequently associated with WCBs and exhibit larger WCB areas.

This leads us to the hypothesis that WCB masks serve as an alternative and computationally cheaper proxy for the contribution of diabatic heating to cyclone intensification. To test this hypothesis, we divided all 247 high-impact cyclones into WCB and non-WCB cyclones based on the median WCB inflow area during the intensification phase. The median ratio of the diabatic contribution to cyclone deepening during the intensification phase is 29% for cyclones with WCBs, compared with 18% for cyclones without WCBs detected by the ML-model ELIAS. For the entire sample, the median diabatic contribution was 25.3% (Figure 2). These results demonstrate that WCB cyclones exhibit a greater diabatic contribution to cyclone intensification, while non-WCB cyclones have a significantly lower average diabatic contribution.

3.4 | Impacts

In this study, we analyse a sample of 247 high-impact cyclones with strong wind gusts over central Europe. The Pearson correlation coefficient of −0.04 of high-impact cyclones between MI ranks (Section 2.2) and the relative contribution of diabatic heating indicates no correlation. This points to a roughly equal distribution of diabatically driven and baroclinically driven cyclones among the top 300 cyclones selected based on their MI rankings. Thus, the diabatically driven cyclones are not the ones with the highest MI, but rather the high-impact cyclones exhibit both diabatically driven and baroclinically driven characteristics. We assess whether the impacts of diabatically and baroclinically driven cyclones differ in terms of precipitation and winds. Diabatically driven cyclones exhibit more precipitation than baroclinically driven cyclones (Figure 9a–d), at −12 h over 1.2 $mm \cdot h^{-1}$ more (Figure 9c). The differences are largest north of the cyclone centres, reflecting the differences in WCB ascent frequencies discussed previously. Using bootstrapping, we tested the significance of the spatial mean precipitation differences between diabatically and baroclinically driven cyclones of the total composite area. The 99% confidence interval for mean differences lies entirely above zero. Thus, precipitation amounts associated with diabatically compared with baroclinically driven cyclones differ significantly. Diabatically driven cyclones exhibit locally stronger surface wind speeds and gusts (Figure 9e–l), particularly between −12 and −0 h, with wind speeds that are up to 6 $m \cdot s^{-1}$ higher (Figure 9g–h) and gusts up to 8 $m \cdot s^{-1}$

1477870x, 0, Downloaded from https://rmets.onlinelibrary.wiley.com/doi/10.1002/qj.70083 by Karlsruher Institut Für Technologie, Wiley Online Library on [07/01/2026]. See the Terms and Conditions (https://onlinelibrary.wiley.com/terms-and-conditions) on Wiley Online Library for rules of use; OA articles are governed by the applicable Creative Commons License

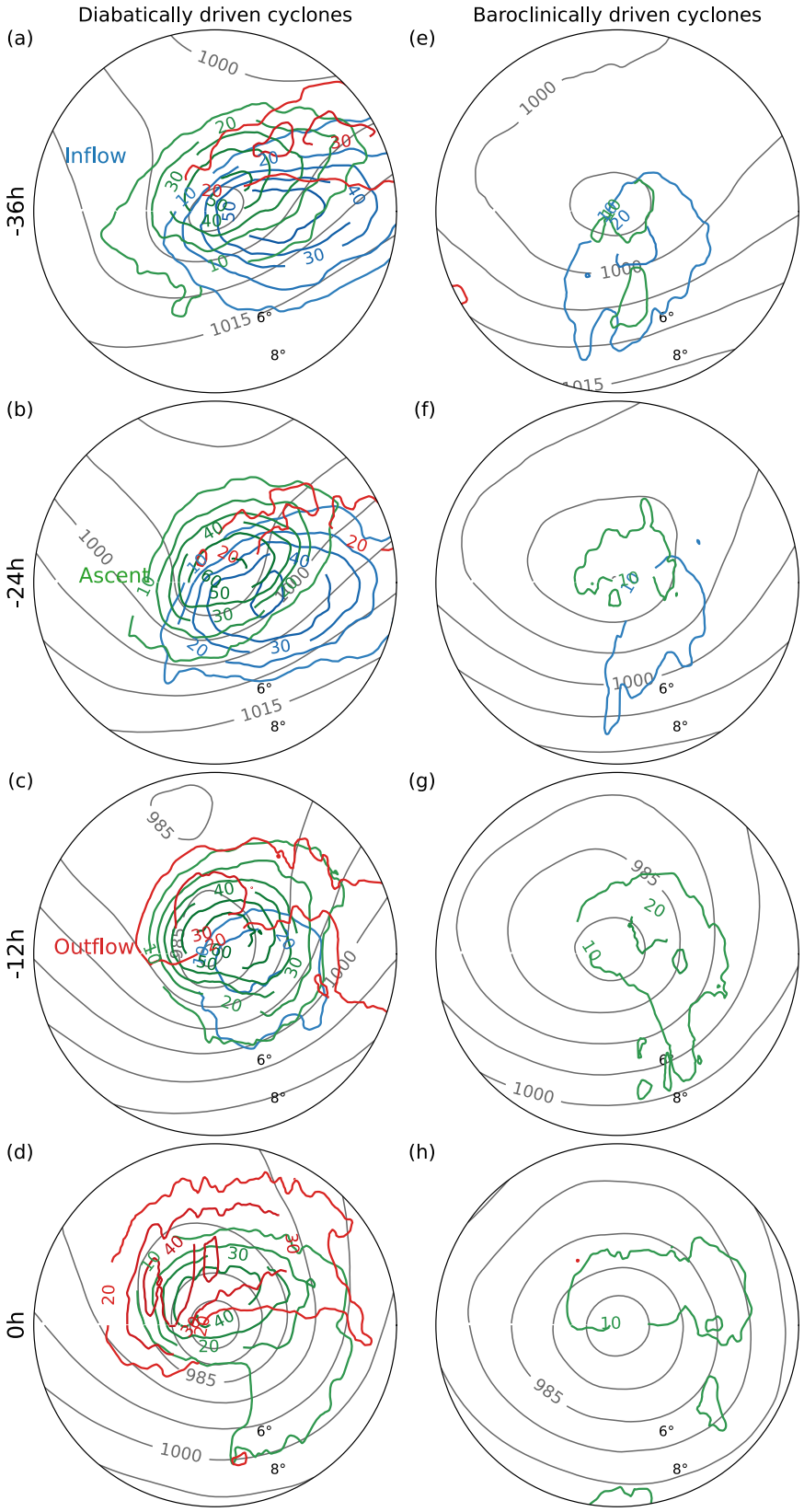

FIGURE 8 Cyclone composites for frequencies of WCB inflow (blue, starting at 10% every 10%), WCB ascent (green, starting at 10% every 10%), and WCB outflow (red, starting at 20% every 10%) for diabatically driven (left column) and baroclinically driven (right column) cyclones at −36, −24, −12, and 0 h relative to peak intensity with a 9° radius around the cyclone centre. [Colour figure can be viewed at wileyonlinelibrary.com]

higher (Figure 9k–l) than those of baroclinically driven cyclones. From −36 and 0 h, the 99% confidence interval for the spatially averaged wind gust differences, and from −24 h to 0 h the wind-speed differences between diabatically and baroclinically driven cyclones, lies above zero. The confidence interval for wind speed at −36 h is above

1477870x, 0, Downloaded from https://rmets.onlinelibrary.wiley.com/doi/10.1002/qj.70083 by Karlsruher Institut Für Technologie, Wiley Online Library on [07/01/2026]. See the Terms and Conditions (https://onlinelibrary.wiley.com/terms-and-conditions) on Wiley Online Library for rules of use; OA articles are governed by the applicable Creative Commons License

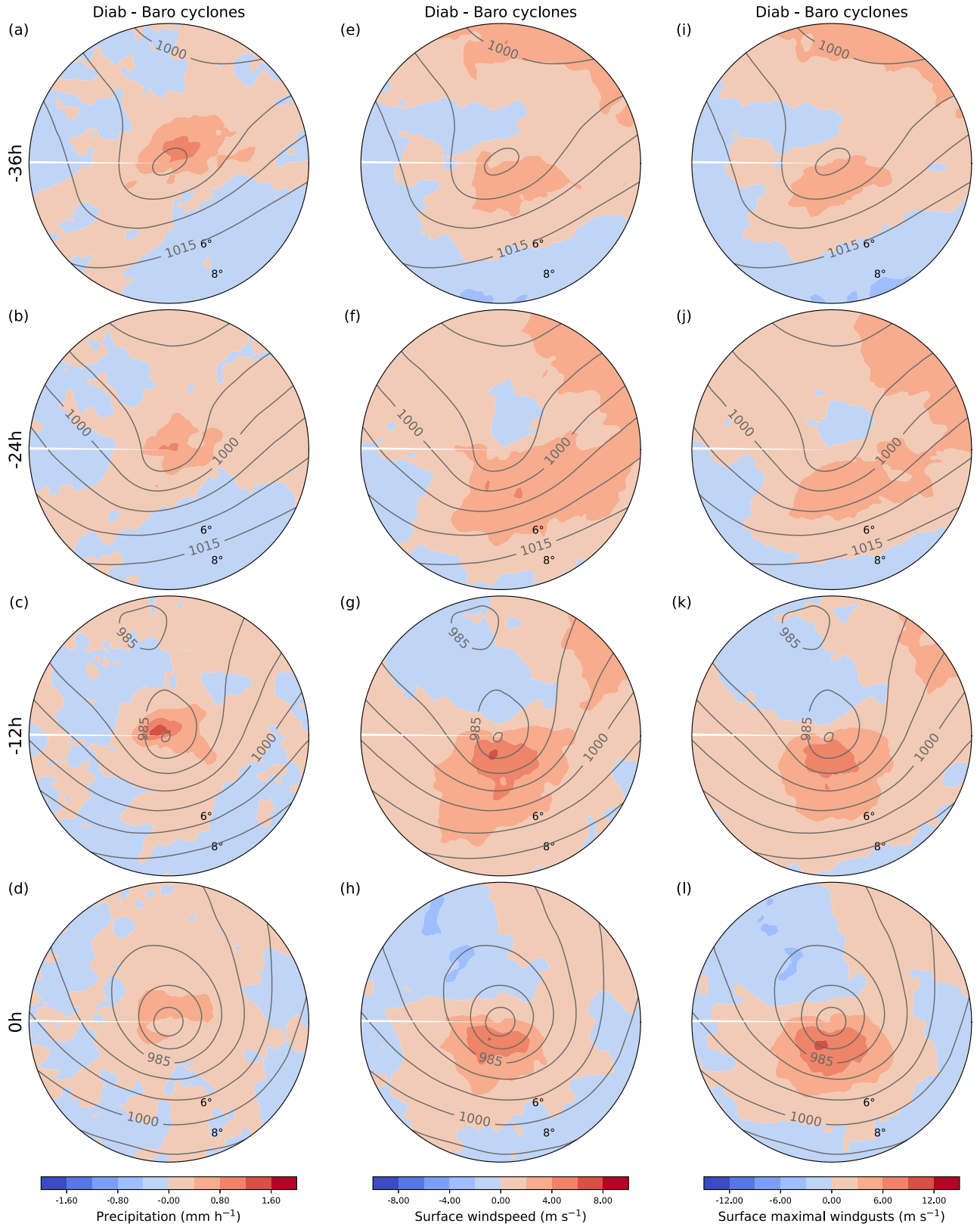

FIGURE 9 Cyclone composites for differences between diabatically (Diab) and baroclinically (Baro) driven cyclones of surface wind speed (shading, in m · s^{-1}), surface wind gusts (shading, in m · s^{-1}), precipitation (shading, in mm · h^{-1}), and diabatically driven cyclone mean sea-level pressure (black contours, every 5 hPa) at −36, −24, −12, and 0 h relative to peak intensity with a 9° radius around the cyclone centre. Absolute composites are shown in the Supporting Information section (Figures S1–S3). [Colour figure can be viewed at wileyonlinelibrary.com]

1477870x, 0, Downloaded from https://rmets.onlinelibrary.wiley.com/doi/10.1002/qj.70083 by Karlsruher Institut Für Technologie, Wiley Online Library on [07/01/2026]. See the Terms and Conditions (https://onlinelibrary.wiley.com/terms-and-conditions) on Wiley Online Library for rules of use; OA articles are governed by the applicable Creative Commons License

zero for the 95% confidence interval. Stronger winds are expected primarily in specific regions, such as the cold front and the warm and cold jets. Accordingly, the differences are largest in the cyclone's warm sector, indicating stronger moisture transport, which may provide additional moisture for the WCBs. Since wind gusts constitute the primary variable used to define the MI Index, this appears to be a contradiction. We argue that the MI Index is calculated within a fixed region, while the composites follow the cyclone centre and show more directly the winds associated with the region around the cyclone centre. In conclusion, diabatically driven cyclones have a higher overall impact, driven by significantly enhanced stronger surface winds and wind gusts. High wind speeds, in particular, show notable differences between diabatically and baroclinically driven cyclones. Also, they are characterised by greater precipitation. This potentially leads to more severe weather events.

4 | SUMMARY AND DISCUSSION

This study examines the characteristics of high-impact cyclones affecting Europe, specifically those with a relatively large diabatic influence versus those with a small diabatic influence. It explores a sample of 247 cyclones, identified from ERA5 cyclone tracks spanning the extended winter seasons between 1979 and 2023. The selection of cyclones is based on peak intensity over central Europe, using the MI to measure impact in terms of wind extremes. The PTE approach is used to assess the role of diabatic processes in cyclone intensification. We group the high-impact cyclone sample into diabatically driven cyclones (with a considerable contribution of diabatic heating to cyclone deepening) and baroclinically driven cyclones (cyclone deepening dominated by horizontal temperature advection). Furthermore, we analyse the frequency and extent of WCBs associated with these cyclones using the ML-model ELIAS to identify WCB masks. Regarding the main research questions raised in the Introduction (Section 1), the main findings are as follows.

1. The magnitude of the diabatic contribution to cyclone intensification of the high-impact cyclones affecting Europe is quantified with the PTE approach. The relative contribution can be substantial in certain cases (over 70%), with a median contribution of 25%, a lower tercile of 20%, and an upper tercile of 31%. Even though the large majority of cyclones are dominated by baroclinic processes (with over 50% contribution), our results show that diabatic heating can indeed be very important for cyclone intensification.
2. Diabatically driven cyclones exhibit a faster intensification than baroclinically driven cyclones, and the overall intensity is similar. Diabatically driven cyclones tend to cross the jet stream, whereas baroclinically driven cyclones typically develop on its northern side. Diabatically driven cyclones exhibit faster propagation speeds and greater northward displacement and tend to form further south, particularly in the Gulf Stream region, where temperatures are generally warmer. Moreover, they develop in an environment with elevated lower-tropospheric specific humidity in the WCB inflow region, which is hypothesised to enhance WCB activity and to contribute to increased precipitation, higher wind gusts, and faster deepening rates.
3. The characteristics of the WCBs are quantified with ELIAS, revealing clear differences between diabatically and baroclinically driven cyclones. Of diabatically driven cyclones, 80% are associated with WCB ascent masks, while only 46% of baroclinically driven cyclones are associated with WCB ascent masks. Diabatically driven cyclones have larger WCB inflow and ascent areas. Moreover, cyclones with more WCB activity have a higher ratio of diabatic heating contributions to intensification. These results suggest that WCB masks are a good and computationally cheaper indicator for the contribution of diabatic heating to cyclone intensification.

Generally, the magnitude of the PTE terms calculated for our cyclone sample agrees well with numbers found in Fink *et al.* (2012) and Pirret *et al.* (2017). Our results are in agreement with Pirret *et al.* (2017), who found a dominance of baroclinic processes in most storms, with up to 60% contribution of diabatic processes in some cases, in agreement with our results. Also, Pirret *et al.* (2017) found no correlation between storm intensity and PTE contributions, consistent with our results. However, unlike their case-based analyses, our study provides the first systematic assessment of diabatic and baroclinic contributions to cyclone deepening in combination with a WCB analysis. A limitation of our study is that the PTE assumes a constant background state, which means that only the eddy effects are considered, while the influence of the background climatology is not accounted for. Still, we argue that the PTE is suitable for quantifying the different processes contributing to cyclone intensification. We find no correlation between the ratio of diabatic contributions to cyclone intensification and the MI within our cyclone sample. It is important to note that our analysis focused exclusively on high-impact cyclones over Europe. The results might differ if we compare the MI across all wintertime cyclones. For example, Stanković *et al.* (2024) found a higher ratio of the diabatic contribution to the pressure drop in extreme

1477870x, 0, Downloaded from https://rmets.onlinelibrary.wiley.com/doi/10.1002/qj.70083 by Karlsruher Institut Für Technologie, Wiley Online Library on [07/01/2026]. See the Terms and Conditions (https://onlinelibrary.wiley.com/terms-and-conditions) on Wiley Online Library for rules of use; OA articles are governed by the applicable Creative Commons License

windstorms compared with moderate ones in the central North Atlantic. Nevertheless, impacts measured in terms of surface wind speed, surface wind gusts, and especially precipitation are larger for our diabatically driven cyclones compared with the baroclinically driven ones. Our hypothesis that cyclones with severe impacts over central Europe exhibit significant contributions from diabatic processes can thus be partly confirmed. We therefore conclude that diabatic heating plays a critical role in rapid cyclone intensification.

Our work systematically contrasts many aspects of the structural differences and drivers of cyclones with a large versus small diabatic heating influence across a large set of cyclones. Consistent with results in Pirret *et al.* (2017), a statistically significant relationship between the diabatic contribution to cyclone intensification and the time the storm spends on the equatorward side of the jet is found in our results. Further northward displacement of cyclones is attributed to latent heating, as noted by Tamarin and Kaspi (2016). In agreement, a greater northward displacement for moist compared with dry idealised cyclone experiments was observed in Coronel *et al.* (2015). The differences in lower-tropospheric winds, MSLP, and jet stream composites between diabatically driven and baroclinically driven cyclones resemble those found between cyclones with and without sting-jet precursors (Gray *et al.*, 2024). A further similarity is that the diabatically driven cyclones with stronger near-surface winds exhibit faster propagation. This consistency is not unexpected, given that the diagnostic they used to identify precursors selects cyclones with strong convective-type atmospheric instabilities, which are more typical of cyclones with large diabatically driven processes. Additionally, our findings suggest that diabatically driven cyclones align more closely with the Shapiro–Keyser cyclone model rather than the Norwegian cyclone model. Consistent with findings by Papritz and Schemm (2013) and Rivière *et al.* (2015), cyclones that cross the jet are more likely to undergo frontal fracture, which is also indicated in our study.

Previous work has shown that cyclone intensity correlates with WCB strength, as PV production through diabatic heating in WCBs contributes significantly to the intensification of rapidly deepening cyclones (Binder *et al.*, 2016), and sensitivity experiments showed that enhanced latent heat release in the WCB leads to more intense cyclones (Booth *et al.*, 2012). This is also reflected in our findings, where cyclones exhibiting a stronger diabatic heating contribution to intensification consistently show increased WCB activity, highlighting the WCB's ability to indicate diabatic processes. A limitation of our analysis is that we cannot compare WCB strength directly, which would have been possible by examining WCB trajectories. While some sensitivity to WCB strength may already be reflected in the comparison between WCB and non-WCB cyclones, a more explicit representation could be achieved by training the ML-model ELIAS not only on WCB inflow, ascent, and outflow masks but also on WCB strength, for example, by using a trajectory-based metric during training. This would allow the model to learn from more detailed information, while retaining the advantage of avoiding computationally expensive trajectory calculations when applied to new data. Moist processes and diabatic heating are important for the storm-track evolution (e.g., Marcheggiani & Spengler, 2023). We find that moisture availability is closely linked to enhanced WCB activity and a stronger diabatic contribution to cyclone intensification. This is in line with Pfahl *et al.* (2014) and Schäfler and Harnisch (2015), who highlighted the importance of moisture availability for diabatic heating in the ascending WCB airstream and for precipitation. Our results align with previous findings showing that increased moisture enhances cyclone intensification rates, extreme surface winds, and precipitation (Booth *et al.*, 2013).

Our work builds the foundation for future work addressing the question of how diabatic heating will affect cyclone characteristics in a changing climate. For example, the diagnostics described in this study enhance our understanding of the role of diabatic processes in cyclone intensification. Specifically, an analysis of the structural differences between diabatically driven and baroclinically driven cyclones can help to identify how cyclone intensification processes interact with each other and address uncertainties regarding the extent to which increased latent heating will feed back to amplify cyclone intensity (Catto *et al.*, 2019). Though the number of cyclones may decrease slightly in a warmer climate (Little *et al.*, 2023; Priestley & Catto, 2020; Ulbrich *et al.*, 2009), their intensity distribution is expected to broaden, resulting in both stronger and weaker storms (Sinclair *et al.*, 2020). Diabatic processes are projected to play an increasingly significant role in cyclone intensification (Chen *et al.*, 2024; Fink *et al.*, 2012). This is also true for impacts, especially in the context of their compound characteristics, namely wet and windy extremes (Chen *et al.*, 2024; Zscheischler *et al.*, 2018). However, uncertainties remain regarding the extent to which increased latent heating will feed back to amplify cyclone intensity (Catto *et al.*, 2019). Additionally, it is unclear how this will interact with surface and upper-tropospheric warming and how these factors will influence cyclone frequency and intensity in the future. This work may also be used to validate climate models and investigate how diabatically and baroclinically driven cyclones are characterised in those models, and thus also to quantify associated risks.

1477870x, 0, Downloaded from https://rmets.onlinelibrary.wiley.com/doi/10.1002/qj.70083 by Karlsruher Institut Für Technologie, Wiley Online Library on [07/01/2026]. See the Terms and Conditions (https://onlinelibrary.wiley.com/terms-and-conditions) on Wiley Online Library for rules of use; OA articles are governed by the applicable Creative Commons License

ACKNOWLEDGEMENTS

The research leading to these results has been performed within the subproject "A6 Intensity and structural changes of extreme midlatitude cyclones in a warming climate" of the ClimXtreme and ClimXtreme2 projects (www.climxtreme.de). ClimXtreme and ClimXtreme2 (01LP1901A, 01LP2322A) are funded by the German Federal Ministry of Research, Technology and Space (BMFTR) within the framework of "Research for Sustainable Development" (FONA). The analysis was carried out on the supercomputer Levante at DKRZ, Hamburg, and datasets provided by DKRZ via the DKRZ data pool were used. This work used resources of the Deutsches Klimarechenzentrum (DKRZ) granted by its Scientific Steering Committee (WLA) under Project IDs bm1159 and bb1152. S. Chirst thanks the RS Stiftung for travel support. J. G. Pinto thanks the AXA research fund for support. We are very grateful to Victoria Sinclair and Joona Corner for providing the script to calculate cyclone composites, and to Ting-Chen Chen for providing the script to calculate the PTE. We thank Sue Gray and one anonymous reviewer for constructive comments, which helped to improve the article. The contribution of J. Quinting is supported by the European Union (ERC, ASPIRE, 101077260). Open Access funding enabled and organized by Projekt DEAL.

DATA AVAILABILITY STATEMENT

ERA5 data used in this study are freely available in the Copernicus Climate Change Service Climate Data Store (doi.org/10.24381/cds.bd0915c6). Cyclone track data are available upon request, and WCB masks will be published upon acceptance.

ORCID

Svenja Christ https://orcid.org/0009-0009-5876-6686
Julian Quinting https://orcid.org/0000-0002-8409-2541
Joaquim G. Pinto https://orcid.org/0000-0002-8865-1769

REFERENCES

Baehr, C., Pouponneau, B., Ayrault, F. & Joly, A. (1999) Dynamical characterization of the FASTEX cyclogenesis cases. *Quarterly Journal of the Royal Meteorological Society*, 125, 3469–3494.

Bengtsson, L., Hodges, K.I., Esch, M., Keenlyside, N., Kornblueh, L., Luo, J.-J. et al. (2007) How may tropical cyclones change in a warmer climate? *Tellus A: Dynamic Meteorology and Oceanography*, 59, 539–561.

Binder, H., Boettcher, M., Joos, H. & Wernli, H. (2016) The role of warm conveyor belts for the intensification of extratropical cyclones in Northern Hemisphere winter. *Journal of the Atmospheric Sciences*, 73, 3997–4020.

Booth, J.F., Thompson, L., Patoux, J. & Kelly, K.A. (2012) Sensitivity of midlatitude storm intensification to perturbations in the sea surface temperature near the Gulf Stream. *Monthly Weather Review*, 140, 1241–1256.

Booth, J.F., Wang, S. & Polvani, L. (2013) Midlatitude storms in a moister world: lessons from idealized baroclinic life cycle experiments. *Climate Dynamics*, 41, 787–802.

Browning, K.A. (1990) Organization of clouds and precipitation in extratropical cyclones. In: Newton, C.W & Holopainen, E.O. (Eds) *Extratropical Cyclones*. Boston, MA: American Meteorological Society.

Browning, K.A. & Roberts, N.M. (1994) Structure of a frontal cyclone. *Quarterly Journal of the Royal Meteorological Society*, 120, 1535–1557.

Büeler, D. & Pfahl, S. (2017) Potential vorticity diagnostics to quantify effects of latent heating in extratropical cyclones. Part I: Methodology. *Journal of the Atmospheric Sciences*, 74, 3567–3590.

Carlson, T.N. (1991) *Mid-latitude weather systems*. Hammersmith, London, New York, NY, USA: HarperCollins Academic.

Catto, J.L., Ackerley, D., Booth, J.F., Champion, A.J., Colle, B.A., Pfahl, S. et al. (2019) The future of midlatitude cyclones. *Current Climate Change Reports*, 5, 407–420.

Catto, J.L., Shaffrey, L.C. & Hodges, K.I. (2010) Can climate models capture the structure of extratropical cyclones? *Journal of Climate*, 23, 1621–1635.

Chang, C.B., Perkey, D.J. & Kreitzberg, C.W. (1982) A numerical study of baroclinic development in a moist atmosphere. *Journal of the Atmospheric Sciences*, 39, 1555–1570.

Chen, T.-C., Braun, C., Voigt, A. & Pinto, J.G. (2024) Changes of intense extratropical cyclone deepening mechanisms in a warmer climate in idealized simulations. *Journal of Climate*, 37, 4703–4722.

Coronel, B., Ricard, D., Rivière, G. & Arbogast, P. (2015) Role of moist processes in the tracks of idealized midlatitude surface cyclones. *Journal of the Atmospheric Sciences*, 72, 2979–2996.

Dacre, H.F. & Gray, S.L. (2009) The spatial distribution and evolution characteristics of North Atlantic cyclones. *Monthly Weather Review*, 137, 99–115.

Dacre, H.F., Hawcroft, M.K., Stringer, M.A. & Hodges, K.I. (2012) An extratropical cyclone atlas: a tool for illustrating cyclone structure and evolution characteristics. *Bulletin of the American Meteorological Society*, 93, 1497–1502.

Dacre, H.F., Martínez-Alvarado, O. & Mbengue, C.O. (2019) Linking atmospheric rivers and warm conveyor belt airflows. *Journal of Hydrometeorology*, 20, 1183–1196.

Danard, M.B. (1964) On the influence of released latent heat on cyclone development. *Journal of Applied Meteorology and Climatology*, 3, 27–37.

Dee, D.P., Uppala, S.M., Simmons, A.J., Berrisford, P., Poli, P., Kobayashi, S. et al. (2011) The ERA-Interim reanalysis: configuration and performance of the data assimilation system. *Quarterly Journal of the Royal Meteorological Society*, 137, 553–597.

Demirdjian, R., Boyle, J., Finocchio, P.M. & Reynolds, C.A. (2023) Preconditioning and intensification of upstream extratropical cyclones through surface fluxes. *Journal of the Atmospheric Sciences*, 80, 1499–1517.

Deveson, A.C.L., Browning, K.A. & Hewson, T.D. (2002) A classification of FASTEX cyclones using a height-attributable quasi-geostrophic vertical-motion diagnostic. *Quarterly Journal of the Royal Meteorological Society*, 128, 93–117.

Dolores-Tesillos, E., Teubler, F. & Pfahl, S. (2022) Future changes in North Atlantic winter cyclones in CESM-LE – Part 1: cyclone

1477870x, 0, Downloaded from https://rmets.onlinelibrary.wiley.com/doi/10.1002/qj.70083 by Karlsruher Institut Für Technologie, Wiley Online Library on [07/01/2026]. See the Terms and Conditions (https://onlinelibrary.wiley.com/terms-and-conditions) on Wiley Online Library for rules of use; OA articles are governed by the applicable Creative Commons License

intensity, potential vorticity anomalies, and horizontal wind speed. *Weather and Climate Dynamics*, 3, 429–448.

Dowdy, A.J. & Catto, J.L. (2017) Extreme weather caused by concurrent cyclone, front and thunderstorm occurrences. *Scientific Reports*, 7, 40359.

Fink, A.H., Brücher, T., Ermert, V., Krüger, A. & Pinto, J.G. (2009) The European storm Kyrill in January 2007: synoptic evolution, meteorological impacts and some considerations with respect to climate change. *Natural Hazards and Earth System Sciences*, 9, 405–423.

Fink, A.H., Pohle, S., Pinto, J.G. & Knippertz, P. (2012) Diagnosing the influence of diabatic processes on the explosive deepening of extratropical cyclones. *Geophysical Research Letters*, 39, L07803.

Flaounas, E., Gray, S.L. & Teubler, F. (2021) A process-based anatomy of Mediterranean cyclones: from baroclinic lows to tropical-like systems. *Weather and Climate Dynamics*, 2, 255–279.

Gray, S.L. & Dacre, H.F. (2006) Classifying dynamical forcing mechanisms using a climatology of extratropical cyclones. *Quarterly Journal of the Royal Meteorological Society*, 132, 1119–1137.

Gray, S.L., Volonté, A., Martínez-Alvarado, O. & Harvey, B.J. (2024) A global climatology of sting-jet extratropical cyclones. *Weather and Climate Dynamics*, 5, 1523–1544.

Hénin, R., Ramos, A.M., Pinto, J.G. & Liberato, M.L.R. (2021) A ranking of concurrent precipitation and wind events for the Iberian Peninsula. *International Journal of Climatology*, 41, 1421–1437.

Hersbach, H., Bell, B., Berrisford, P., Hirahara, S., Horányi, A., Muñoz-Sabater, J. et al. (2020) The ERA5 global reanalysis. *Quarterly Journal of the Royal Meteorological Society*, 146, 1999–2049.

Hoskins, B.J. & Hodges, K.I. (2002) New perspectives on the Northern Hemisphere winter storm tracks. *Journal of the Atmospheric Sciences*, 59, 1041–1061.

Joos, H. & Wernli, H. (2012) Influence of microphysical processes on the potential vorticity development in a warm conveyor belt: a case-study with the limited-area model COSMO. *Quarterly Journal of the Royal Meteorological Society*, 138, 407–418.

Klawa, M. & Ulbrich, U. (2003) A model for the estimation of storm losses and the identification of severe winter storms in Germany. *Natural Hazards and Earth System Sciences*, 3, 725–732.

Knippertz, P. & Fink, A.H. (2008) Dry-season precipitation in Tropical West Africa and its relation to forcing from the extratropics. *Monthly Weather Review*, 136, 3579–3596.

Knippertz, P., Fink, A.H. & Pohle, S. (2009) Reply. *Monthly Weather Review*, 137, 3151–3157.

Little, A.S., Priestley, M.D.K. & Catto, J.L. (2023) Future increased risk from extratropical windstorms in Northern Europe. *Nature Communications*, 14, 4434.

Ludwig, P., Pinto, J.G., Reyers, M. & Gray, S.L. (2014) The role of anomalous SST and surface fluxes over the southeastern North Atlantic in the explosive development of windstorm Xynthia. *Quarterly Journal of the Royal Meteorological Society*, 140, 1729–1741.

Madonna, E., Wernli, H., Joos, H. & Martius, O. (2014) Warm conveyor belts in the ERA-Interim dataset (1979–2010). Part I: climatology and potential vorticity evolution. *Journal of Climate*, 27, 3–26.

Marcheggiani, A. & Spengler, T. (2023) Diabatic effects on the evolution of storm tracks. *Weather and Climate Dynamics*, 4, 927–942.

Moemken, J., Messori, G. & Pinto, J.G. (2024) Windstorm losses in Europe - what to gain from damage datasets. *Weather and Climate Extremes*, 44, 100661.

Murray, R.J. & Simmonds, I. (1991) A numerical scheme for tracking cyclone centres from digital data. Part II: application to January and July general circulation model simulations. *Australian Meteorological Magazine*, 39, 167–180.

Neu, U., Akperov, M.G., Bellenbaum, N., Benestad, R., Blender, R., Caballero, R. et al. (2013) IMILAST: a community effort to intercompare extratropical cyclone detection and tracking algorithms. *Bulletin of the American Meteorological Society*, 94, 529–547.

Papritz, L. & Schemm, S. (2013) Development of an idealised downstream cyclone: Eulerian and Lagrangian perspective on the kinetic energy. *Tellus A: Dynamic Meteorology and Oceanography*, 65, 19539.

Parker, D.J. (1998) Secondary frontal waves in the north Atlantic region: a dynamical perspective of current ideas. *Quarterly Journal of the Royal Meteorological Society*, 124, 829–856.

Pfahl, S. (2014) Characterising the relationship between weather extremes in Europe and synoptic circulation features. *Natural Hazards and Earth System Sciences*, 14, 1461–1475.

Pfahl, S., Madonna, E., Boettcher, M., Joos, H. & Wernli, H. (2014) Warm conveyor belts in the ERA-Interim dataset (1979-2010). Part II: moisture origin and relevance for precipitation. *Journal of Climate*, 27, 27–40.

Pinto, J.G., Gómara, I., Masato, G., Dacre, H.F., Woollings, T. & Caballero, R. (2014) Large-scale dynamics associated with clustering of extratropical cyclones affecting Western Europe. *Journal of Geophysical Research: Atmospheres*, 119, 704–719.

Pinto, J.G., Karremann, M.K., Born, K., Della-Marta, P.M. & Klawa, M. (2012) Loss potentials associated with European windstorms under future climate conditions. *Climate Research*, 54, 1–20.

Pinto, J.G., Spangehl, T., Ulbrich, U. & Speth, P. (2005) Sensitivities of a cyclone detection and tracking algorithm: individual tracks and climatology. *Meteorologische Zeitschrift*, 14, 823–838.

Pinto, J.G., Zacharias, S., Fink, A.H., Leckebusch, G.C. & Ulbrich, U. (2009) Factors contributing to the development of extreme North Atlantic cyclones and their relationship with the NAO. *Climate Dynamics*, 32, 711–737.

Pirret, J.S.R., Knippertz, P. & Trzeciak, T.M. (2017) Drivers for the deepening of severe European windstorms and their impacts on forecast quality. *Quarterly Journal of the Royal Meteorological Society*, 143, 309–320.

Plant, R.S., Craig, G.C. & Gray, S.L. (2003) On a threefold classification of extratropical cyclogenesis. *Quarterly Journal of the Royal Meteorological Society*, 129, 2989–3012.

Pohle, S. (2010) *Synoptische und dynamische Aspekte tropisch-extratropischer Wechselwirkungen: Drei Fallstudien von Hitzetiefentwicklungen über Westafrika während des AMMA-Experiments 2006*. Ph.D. thesis, Universität zu Köln. https://kups.ub.uni-koeln.de/3157/

Priestley, M.D.K. & Catto, J.L. (2020) Future changes in the extratropical storm tracks and cyclone intensity, wind speed, and structure. *Weather and Climate Dynamics*, 3, 337–360.

Priestley, M.D.K., Dacre, H.F., Shaffrey, L.C., Schemm, S. & Pinto, J.G. (2020) The role of secondary cyclones and cyclone families for the North Atlantic storm track and clustering over Western Europe. *Quarterly Journal of the Royal Meteorological Society*, 146, 1184–1205.

Quinting, J.F. & Grams, C.M. (2022) EuLerian identification of ascending airstreams (ELIAS 2.0) in numerical weather prediction and climate models – Part 1: development of deep learning model. *Geoscientific Model Development*, 15, 715–730.

1477870x, 0, Downloaded from https://rmets.onlinelibrary.wiley.com/doi/10.1002/qj.70083 by Karlsruher Institut Für Technologie, Wiley Online Library on [07/01/2026]. See the Terms and Conditions (https://onlinelibrary.wiley.com/terms-and-conditions) on Wiley Online Library for rules of use; OA articles are governed by the applicable Creative Commons License

Quinting, J.F., Grams, C.M., Oertel, A. & Pickl, M. (2022) EuLerian identification of ascending airstreams (ELIAS 2.0) in numerical weather prediction and climate models – Part 2: model application to different datasets. *Geoscientific Model Development*, 15, 731–744.

Rivière, G., Arbogast, P. & Joly, A. (2015) Eddy kinetic energy redistribution within windstorms Klaus and Friedhelm. *Quarterly Journal of the Royal Meteorological Society*, 141, 925–938.

Robertson, F.R. & Smith, P.J. (1983) The impact of model moist processes on the energetics of extratropical cyclones. *Monthly Weather Review*, 111, 723–744.

Rudeva, I. & Gulev, S.K. (2007) Climatology of cyclone size characteristics and their changes during the cyclone life cycle. *Monthly Weather Review*, 135, 2568–2587.

Schäfler, A. & Harnisch, F. (2015) Impact of the inflow moisture on the evolution of a warm conveyor belt. *Quarterly Journal of the Royal Meteorological Society*, 141, 299–310.

Schultz, D.M. (2001) Reexamining the cold conveyor belt. *Monthly Weather Review*, 129, 2205–2225.

Schultz, D.M., Bosart, L.F., Colle, B.A., Davies, H.C., Dearden, C., Keyser, D. et al. (2019) Extratropical cyclones: a century of research on meteorology's centerpiece. *Meteorological Monographs*, 59, 16.1–16.56.

Sinclair, V.A. & Catto, J.L. (2023) The relationship between extra-tropical cyclone intensity and precipitation in idealised current and future climates. *Weather and Climate Dynamics*, 4, 567–589.

Sinclair, V.A., Rantanen, M., Haapanala, P., Räisänen, J. & Järvinen, H. (2020) The characteristics and structure of extra-tropical cyclones in a warmer climate. *Weather and Climate Dynamics*, 1, 1–25.

Stanković, A., Messori, G., Pinto, J.G. & Caballero, R. (2024) Large-scale perspective on extreme near-surface winds in the central North Atlantic. *Weather and Climate Dynamics*, 5, 821–837.

Tamarin, T. & Kaspi, Y. (2016) The poleward motion of extratropical cyclones from a potential vorticity tendency analysis. *Journal of the Atmospheric Sciences*, 73, 1687–1707.

Ulbrich, U., Leckebusch, G.C. & Pinto, J.G. (2009) Extra-tropical cyclones in the present and future climate: a review. *Theoretical and Applied Climatology*, 96, 117–131.

Wernli, H. (1997) A Lagrangian-based analysis of extratropical cyclones. II: a detailed case-study. *Quarterly Journal of the Royal Meteorological Society*, 123, 1677–1706.

Wernli, H., Dirren, S., Liniger, M.A. & Zillig, M. (2002) Dynamical aspects of the life cycle of the winter storm Lothar (24-26 December 1999). *Quarterly Journal of the Royal Meteorological Society*, 128, 405–429.

Wernli, H. & Gray, S.L. (2024) The importance of diabatic processes for the dynamics of synoptic-scale extratropical weather systems - a review. *Weather and climate dynamics*, 5, 1299–1408.

Wernli, H. & Schwierz, C. (2006) Surface cyclones in the ERA-40 dataset (1958-2001). Part I: novel identification method and global climatology. *Journal of the Atmospheric Sciences*, 63, 2486–2507.

Xoplaki, E., Ellsäßer, F., Grieger, J., Nissen, K.M., Pinto, J.G., Augenstein, M. et al. (2025) Compound events in Germany in 2018: drivers and case studies. *Natural Hazards and Earth System Sciences*, 25, 541–564.

Zscheischler, J., Martius, O., Westra, S., Bevacqua, E., Raymond, C., Horton, R.M. et al. (2020) A typology of compound weather and climate events. *Nature Reviews Earth & Environment*, 1, 333–347.

Zscheischler, J., Westra, S., van den Hurk, B.J.J.M., Seneviratne, S.I., Ward, P.J., Pitman, A. et al. (2018) Future climate risk from compound events. *Nature Climate Change*, 8, 469–477.

SUPPORTING INFORMATION

Additional supporting information can be found online in the Supporting Information section at the end of this article.

How to cite this article: Christ, S., Quinting, J. & Pinto, J.G. (2025) Characteristics of diabatically influenced cyclones with high wind damage potential in Europe. *Quarterly Journal of the Royal Meteorological Society*, e70083. Available from: https://doi.org/10.1002/qj.70083

1477870x, 0, Downloaded from https://rmets.onlinelibrary.wiley.com/doi/10.1002/qj.70083 by Karlsruher Institut Für Technologie, Wiley Online Library on [07/01/2026]. See the Terms and Conditions (https://onlinelibrary.wiley.com/terms-and-conditions) on Wiley Online Library for rules of use; OA articles are governed by the applicable Creative Commons License